

REPORT DOCUMENTATION PAGE				Form Approved OMB No. 0704-0188	
<small>Public reporting burden for this collection of information is estimated to average 1 hour per response, including the time for reviewing instructions, searching existing data sources, gathering and maintaining the data needed, and completing and reviewing the collection of information. Send comments regarding this burden estimate or any other aspect of this collection of information, including suggestions for reducing the burden, to Department of Defense, Washington Headquarters Services, Directorate for Information Operations and Reports (0704-0188), 1215 Jefferson Davis Highway, Suite 1204, Arlington, VA 22202-4302. Respondents should be aware that notwithstanding any other provision of law, no person shall be subject to any penalty for failing to comply with a collection of information if it does not display a currently valid OMB control number. PLEASE DO NOT RETURN YOUR FORM TO THE ABOVE ADDRESS.</small>					
1. REPORT DATE (DD-MM-YYYY) 12-02-2004		2. REPORT TYPE Final Report		3. DATES COVERED (From – To) 22 August 2002 - 22-Aug-03	
4. TITLE AND SUBTITLE Supersonic Turbulent Fuel-Air Mixing				5a. CONTRACT NUMBER FA8655-02-M4078	
				5b. GRANT NUMBER	
				5c. PROGRAM ELEMENT NUMBER	
6. AUTHOR(S) Professor Fadl Moukalled				5d. PROJECT NUMBER	
				5d. TASK NUMBER	
				5e. WORK UNIT NUMBER	
7. PERFORMING ORGANIZATION NAME(S) AND ADDRESS(ES) American University of Beirut ME Dept. PO Box: 11-0236 Beirut Lebanon				8. PERFORMING ORGANIZATION REPORT NUMBER N/A	
9. SPONSORING/MONITORING AGENCY NAME(S) AND ADDRESS(ES) EOARD PSC 802 BOX 14 FPO 09499-0014				10. SPONSOR/MONITOR'S ACRONYM(S)	
				11. SPONSOR/MONITOR'S REPORT NUMBER(S) SPC 02-4078	
12. DISTRIBUTION/AVAILABILITY STATEMENT Approved for public release; distribution is unlimited.					
13. SUPPLEMENTARY NOTES					
14. ABSTRACT <p>This report results from a contract tasking American University of Beirut as follows: The contractor will numerically investigate turbulent fuel-air mixing in a supersonic stream. The fuel injection angle will be varied from 0 to 90 degrees (relative to the air stream) and the air stream Mach number will be varied from 2 to 5. A finite volume pressure based method capable of modeling turbulent multi-phase flow at all speeds will be developed and used. The convergence rate will be accelerated using a full non-linear multi-grid method. The discretization will use a second order scheme for diffusion and a pseudo-third order bounded scheme for convection. Turbulence will be modeled using two-equation models (k-e, k-w, and SST) with suitable modifications to account for interaction between the phases. A comparison with available experimental and numerical results will be performed.</p>					
15. SUBJECT TERMS EOARD, Supersonic Injection, CFD					
16. SECURITY CLASSIFICATION OF:			17. LIMITATION OF ABSTRACT UL	18. NUMBER OF PAGES	19a. NAME OF RESPONSIBLE PERSON WAYNE A. DONALDSON
a. REPORT UNCLAS	b. ABSTRACT UNCLAS	c. THIS PAGE UNCLAS			19b. TELEPHONE NUMBER <i>(Include area code)</i> +44 (0)20 7514 4299

Final Report On:

Supersonic Turbulent Fuel-Air Mixing and Evaporation

(FA8655-02-M4078)

Submitted to:

European Office of Aerospace Research and Development
(EOARD)

by

F. Moukalled
American University of Beirut,
Faculty of Engineering & Architecture,
Mechanical Engineering Department,
P.O.Box 11-0236
Beirut - Lebanon

Address all correspondence to F. Moukalled,
email: memouk@aub.edu.lb

October 20, 2003

Abstract

This work is concerned with the formulation, implementation, and testing, of an all speed numerical procedure for the simulation of turbulent mixing and evaporation of droplets. The numeric is based on a Multi-fluid Eulerian formulation, with a pressure-based fully conservative Finite Volume method equally applicable in the subsonic, transonic, and supersonic regimes, for the discrete and continuous phases. Three two-equation turbulence models are implemented and tested, with modifications to account for compressibility at high speeds. The models are the k - ϵ , k - ω , and more recent Shear Stress Transport (SST) models. The code, written in the FORTRAN computer language, is supplied with a number of ready to run cases. Two configurations involving stream-wise and cross-stream spraying are investigated and solutions for evaporation and mixing in the subsonic and supersonic regimes for droplets sprayed in laminar and turbulent flow streams, are generated over a wide range of operating conditions. Results, displayed in the form of contour plots and axial profiles, reveal the degree of penetration of the injected droplet within the supersonic gas phase, and the rate of evaporation as a function of inlet gas temperature, inlet droplet temperature, and/or the length of the domain.

Key-words: evaporation, mixing, turbulence, phase change, multi-phase flow.

Nomenclature

$A_p^{(k)}, \dots$	coefficients in the discretized equation for $\phi^{(k)}$.
$B_p^{(k)}$	source term in the discretized equation for $\phi^{(k)}$.
$\mathbf{B}^{(k)}$	body force per unit volume of fluid/phase k.
cfh,cfm	correction coefficient for mass and heat transport in droplet model.
$C_\rho^{(k)}$	coefficient equals to $1 / R^{(k)} T^{(k)}$.
C_D	drag coefficient.
C_1, C_2, C_3	turbulence model constants.
$\mathbf{D}_p^{(k)}[\phi^{(k)}]$	the Matrix \mathbf{D} operator.
F^D	drag force.
F_1, F_2	blending functions used in the SST turbulence model.
$H_p[\phi^{(k)}]$	the H operator.
$\mathbf{H}_p[\mathbf{u}^{(k)}]$	the vector form of the H operator.
$\mathbf{I}^{(k)}$	inter-phase momentum transfer.
$\mathbf{J}_f^{(k)D}$	diffusion flux of $\phi^{(k)}$ across cell face 'f'.
$\mathbf{J}_f^{(k)C}$	convection flux of $\phi^{(k)}$ across cell face 'f'.
\dot{m}_d	mass rate of droplet evaporation.
\dot{M}_d	volumetric mass rate of droplet evaporation.
MW_k	Molecular weight of fluid/phase k.
P	pressure.
$\text{Pr}_{(k)}, \text{Pr } t_{(k)}$	laminar and turbulent Prandtl number of fluid/phase k.

$\dot{q}_{(k)}$	heat generated per unit volume of fluid/phase k.
$Q_{(k)}$	general source term of fluid/phase k.
$R_{(k)}$	gas constant for fluid/phase k.
Re_d	Reynolds number based on the droplet diameter.
\mathbf{S}_f	surface vector.
Sc	Schmidt Number.
t	time.
T	temperature of fluid/phase k.
U_f	interface flux velocity $(\mathbf{v}_f^{(k)} \cdot \mathbf{S}_f)$.
\mathbf{u}	velocity vector.
u, v	velocity components in x- and y-direction, respectively.
X	Mole fraction.
Y	Mass fraction.

GREEK SYMBOLS

α	volume fraction.
$\beta_{(k)}$	thermal expansion coefficient for phase/fluid k.
δt	time step.
ρ	density.
$\bar{\tau}$	the stress tensor.
λ	conductivity coefficient.
Γ	diffusion coefficient.
ϕ	general scalar quantity.

Δh latent heat.

$\Delta_P [\phi_{(k)}]$ the Δ operator.

$\mu, \mu_{turb}, \mu_{eff}$ laminar, turbulent and effective viscosity of fluid/phase k.

Ω cell volume.

σ_1, σ_2 turbulence model constants.

SUBSCRIPTS

d refers to the droplet discrete liquid phase.

E refers to energy equation.

g refers to the gas phase.

k refers to turbulent kinetic energy equation.

nb refers to the east, west, ... face of a control volume.

NB refers to the East, West, ... neighbors of the main grid point.

P refers to the P grid point.

s refers to the droplet surface condition.

sat refers to the saturation condition.

ϵ refers to turbulent eddy dissipation equation.

ω refers to turbulent eddy frequency equation.

vap,g refers to the vapor specie in the gas phase.

SUPERSCRIPTS

- C refers to convection contribution.
- D refers to diffusion contribution.
- (k) refers to the kth fluid/phase.
- ^ refers to variable evaluated at reference conditions.
- Old refers to values from the previous time step.

Introduction

BACKGROUND

Recently there has been a revived interest in the supersonic injection of liquids, particularly with respect to fuel injection techniques for hypersonic programs. These designs require air-breathing engines capable of supersonic combustion. The scramjet (supersonic combustion ramjet), appears at present to be the only practical engine for these types of applications since it is able to produce useful thrust at hypersonic flight Mach numbers, using supersonic flow through the combustor. Hydrocarbon-fueled scramjet engines are of particular interest because of their dense, non-cryogenic, easily storable fuels. The scramjet concept itself is fairly old, and was the subject of studies throughout the 1960s and again in the 1980s. However, its coming to fruition depends among other things on the development of numerical tools for the simulation of its supersonic combustion process and related phenomena. More specifically effective disruption and mixing of hydrocarbon fuels in a supersonic flow is a crucial ingredient for the success of any scramjet design. Three key issues govern the performance of the liquid injection process in the scramjet engine, namely: the penetration of the fuel into the free-stream, the atomization of the injected fuel drops, and the level of fuel/air mixing [1]. It is important for the fuel to penetrate effectively into the free-stream so that the combustion process produces an even temperature distribution. If the fuel does not penetrate sufficiently into the free-stream, the combustion will mostly occur along the surface of the combustor (or injector rake), causing inefficient combustor operation and increased cooling problems. Rapid atomization of the fuel is also required for efficient combustion. Increased atomization of the liquid fuel results in increased fuel/air mixing which allows a higher percentage of the fuel to be burnt in the short time before the entire mixture passes out of the combustor (generally on the order of 1 ms).

OBJECTIVES

Approaches for the simulation of droplet transport and evaporation in combustion systems can be classified under two categories, namely the Lagrangian and Eulerian methods. Within both methods the gaseous phase is calculated by solving the Navier-Stokes equations with a standard discretization method such as the Finite Volume Method. In the **Lagrangian** approach [2, 3], the spray is represented by discrete droplets which are advected explicitly through the computational domain while accounting for evaporation and other phenomena. Due to the large number of droplets in a spray, each discrete computational droplet is made to represent a number of physical droplets averaging their characteristics. The equations of motion of each droplet are a set of ordinary differential equations (ODE) which are solved using an ODE solver, a numerical procedure different from that of the continuous phase. To account for the interaction between the gaseous phase and the spray, several iterations of alternating solutions of the gaseous phase and the spray have to be conducted.

Therefore, the computational effort for strongly interacting two-phase flows with the Lagrangian method is rather large. Furthermore, for turbulent flow simulation the above model has to be augmented with a stochastic or Monte-Carlo approach. In the **Eulerian** approach [3,4], the evaporating spray is treated as an interacting and interpenetrating continuum, in analogy to the continuum approach of single phase flows, each phase is described by a set of transport equations for mass, momentum and energy extended by interfacial exchange terms. This description allows the gaseous phase and the spray to be discretized by the same method, and therefore to be solved by the same numerical procedure. Because of the presence of multiple phases a multiphase algorithm is used rather than a single-phase one.

In this project we were interested in developing the numeric foundation for the simulation of supersonic combustion, more specifically to develop a code for the simulation of supersonic droplet evaporation and mixing. This was achieved through a multi-fluid all speed pressure-based finite volume flow solver in which a droplet evaporation model was implemented. Three two equations turbulence models have been considered to account for the droplet and gas turbulence, all modified for supersonic flows. These are the $k-\epsilon$ [5], the $k-\omega$ [6] and the SST [7] models for the gas phase. Droplet turbulence is estimated using an algebraic model based on the Boussinesq approach. The model as it stands does not account for droplet breakup or coagulation, but different droplet sizes are accounted for. The use of an Eulerian approach has many advantages: same validated numeric used for all phases, ease of implementation of acceleration techniques (such as multi-grid), improvements to code are carried over to all phases.

The model developed and implemented in this project accounts for the heating and evaporation of multiple size droplets. The interaction of the gas and droplet phases is accounted for by using a two-phase multi-component Eulerian approach. The implementation has been done for multi-fluid flow at all speeds, and forms a solid foundation for the future study of the more general problem of fuel mixing and combustion. An in-house all-speed multiphase finite volume CFD code is used to compute both the gas flow field and the disperse droplets phase.

PLAN OF REPORT

In what follows detailed derivations of the governing equations for droplet transport and evaporation are presented. Then, results obtained are discussed. Computations have been performed for subsonic, supersonic, laminar, and turbulent flows.

Governing Equations

INTERPENETRATING MEDIA

When describing multiphase flow phenomena it is implied that more than one phase exist within a small volume at any particular time. This view rests on the idea of time and space averaging and implies the following:

1. Any small volume can be regarded as containing a volume fraction $\alpha^{(k)}$ of the k^{th} phase, so that, if there are n phases then

$$\sum_{k=1}^n \alpha^{(k)} = 1 \quad (1)$$

2. The mass flow rate of any phase across any elementary surface within the domain at any time can be expressed in terms of the quantity $\alpha^{(k)} \rho^{(k)} \mathbf{v}^{(k)}$ where $\rho^{(k)}$ is the density of the k^{th} phase and $\mathbf{v}^{(k)}$ is the local value of the velocity vector of that phase.
3. When the content of the finite volume and the flow rates across finite areas are to be computed over finite time intervals, a suitable averaging over space and time will be carried out.

Observance of these rules amounts to treating each phase as a continuum in the space under consideration, which requires choosing a proper scale for the control volume used, or a Representative Elementary Volume (REV).

For a multi-phase system the equations are derived over a REV within which the different phases are present. The scale of the modeled phases has to be smaller than the REV. An extensive review of this averaging approach can be found, for example, in Hassanizadeh [8,9].

Except for the near region of the injector where the spray is dense, the volume fraction of the spray is low. For this dilute two-phase flow regime, interaction between droplets can be neglected. Starting from the Navier-Stokes equations, instantaneous transport equations for the gas and droplet phases can be derived either by spatial, temporal, or ensemble averaging. However, these transport equations can only be used for the description of sprays in laminar gas flows. Since combustors generally operate in the turbulent flow regime, the system of equations is extended by introducing turbulent fluctuations of the transport quantities followed by Reynolds averaging of the equations. For the gaseous phase, three two-equations models were employed, namely the k - ϵ of Spalding and Launder [5,10], the k - ω of Wilcox [6] and finally the SST model of Menter [7], all modified to account for compressibility effects at high speed flows. An algebraic model based on a Boussinesq [11] approach approximates the turbulence terms in the droplet phase transport equations. The interacting flow fields are described by the transport equations described in the subsequent sections.

Geometric Conservation Equation

The volume fractions α_g and α_d , for the gas and droplet phases respectively, are a result of the averaging process. For the two-phase flow considered they are characterized by the condition:

$$\alpha_d + \alpha_g = 1; \quad \alpha_d \ll 1 \quad (2)$$

GAS EQUATIONS

Since we are simulating evaporation in the turbulent flow regime, the system of transport equations is extended by introducing turbulent fluctuations of the transport quantities followed by Reynolds averaging of the equations. The continuity momentum and energy equations for the gas phase, composed of two species namely air and vapor, are generally written as described below.

Mass Conservation

The mass conservation equation is given by:

$$\frac{\partial}{\partial t}(\alpha_g \rho_g) + \nabla \cdot (\alpha_g \mathbf{v}_g \rho_g) = \dot{M}_{vap,g} \quad (3)$$

where α_g , \mathbf{v}_g , and ρ_g are, respectively, the volume fraction, velocity, and density of the gas phase. The density is computed from the air and vapor densities as:

$$\frac{1}{\rho_g} = \sum_{\sim k=(air,vap)} \frac{Y^{(k)}}{\rho^{(k)}} \quad (4)$$

where $Y^{(k)}$ and $\rho^{(k)}$ are the mass fraction and density, respectively, of the k^{th} species, and $\sim k=(air,vap)$ indicates a summation of k over the *air* and *vapor* species.

The density can also be obtained from the ideal gas relation as:

$$\rho_g = \frac{P}{R_g T_g} = \frac{P}{(R_0 / MW_g) T_g} = \frac{P}{\left(\frac{R_0}{MW_g} \right) T_g} = \frac{P}{R_0 \left(\sum_{\sim k=(air,vap)} \frac{Y^{(k)}}{MW^{(k)}} \right) T_g} \quad (5)$$

In equation (3), the source term is due to the evaporation of the fluid droplets and is thus equal to the volumetric mass rate of droplet evaporation, thus we have:

$$\dot{M}_g = \dot{M}_{vap,g} = -\dot{M}_d \quad (6)$$

Momentum Conservation

The momentum conservation equation of the gas phase is written as

$$\frac{\partial}{\partial t}(\alpha_g \rho_g \mathbf{v}_g) + \nabla \cdot (\alpha_g \rho_g \mathbf{v}_g \mathbf{v}_g) = -\alpha_g \nabla p + \nabla \cdot \overline{\overline{\boldsymbol{\tau}}_g} + \mathbf{F}_g^B + \mathbf{F}_g^D + \dot{M}_{vap,g} \mathbf{v}_d \quad (7)$$

where \mathbf{F}^B and \mathbf{F}^D are body and drag forces respectively, for the case of the gas phase the body force can be neglected, while the drag force due to liquid droplets is written as:

$$F_g^D = -\frac{3}{4}\alpha_d\rho_g\frac{C_D}{D}\|\mathbf{v}_d - \mathbf{v}_g\|(\mathbf{v}_g - \mathbf{v}_d) \quad (8)$$

where D is the droplet diameter and the aerodynamic drag coefficient is given by [11]:

$$C_D = 0.36 + \frac{24}{\text{Re}_d} + \frac{5.48}{\text{Re}_d^{0.573}} \quad (9)$$

with Re_d being the droplet Reynolds Number defined as:

$$\text{Re}_d = \frac{\rho_g\|\mathbf{v}_d - \mathbf{v}_g\|D_d}{\mu_g} \quad (10)$$

The stress tensor is written as

$$\bar{\tau} = \alpha_g\mu_{\text{eff}}\left(\nabla\mathbf{v} + \nabla\mathbf{v}^T - \frac{2}{3}(\nabla\cdot\mathbf{v})\mathbf{I}\right) \quad (11)$$

where

$$\mu_{\text{eff}} = \mu + \mu_{\text{turb}} \quad (12)$$

Turbulence Models in the Primary Gas phase

The modeling of turbulence in multiphase flows is an ongoing research area. As in single-phase flows there is no particular model that can accurately predict turbulence over a wide range of flows, therefore various formulations are needed to cover the numerous types of multiphase flows. Furthermore research in multiphase turbulence is still in its infancy as compared to the work accomplished in single flow turbulence, and turbulence models are, understandably, still based on extensions of single flow turbulence models. Of the different groups of turbulence models, the eddy viscosity models are those used in the majority of turbulent multiphase simulations. In this respect, two different strategies are employed: (i) a dispersed formulation in which the turbulence quantities in the dispersed phase are based on the turbulence model of the continuous phase [13-18]; and (ii) a phasic formulation in which a set of turbulence model equations are solved for each phase [19].

As the focus of the present work is on a special type of disperse flows, namely the flow of sprayed droplets and as these generally operate in the turbulent flow regime, the system of transport equations need to be extended by introducing turbulent fluctuations followed by some averaging procedure (Favre or Reynolds averaging). For the current application, three two-equation turbulence models (k - ϵ , k - ω , and SST) are employed for the continuous phase to represent the transport terms resulting from correlations of fluctuating quantities, while for the dispersed phase the turbulence terms are approximated by an algebraic model based on a Boussinesq approach as described later.

Two-equation turbulence models are the best-known and most widely used models in industrial applications. Amongst these the k - ϵ model of Launder [5,10] is the most widely used. Although a number of additional two-equation models have been developed over the years, only one of these models has gained significant attention and challenged the dominance of the k - ϵ model, namely the k - ω model of Wilcox [6].

For both models, a number of modifications and improvements are available, which greatly extend their applicability.

k-ε model

The well-known k-ε [5] model is based on the Boussinesq approximation with the turbulent viscosity formulated as:

$$\mu_{turb(k-\epsilon),g} = \rho_g C_\mu \frac{k_g^2}{\epsilon_g} \quad (13)$$

where the turbulent kinetic energy k_g and the turbulent energy dissipation rate ϵ_g are computed using:

$$\frac{\partial}{\partial t}(\alpha_g \rho_g k_g) + \nabla \cdot (\alpha_g \rho_g \mathbf{v}_g k_g) = \nabla \cdot (\alpha_g \mu_{eff,k,g} \nabla k_g) + \alpha_g (P_k - \rho_g \epsilon_g) + S_{k,d} \quad (14)$$

$$\frac{\partial}{\partial t}(\alpha_g \rho_g \epsilon_g) + \nabla \cdot (\alpha_g \rho_g \mathbf{v}_g \epsilon_g) = \nabla \cdot (\alpha_g \mu_{eff,\epsilon,g} \nabla \epsilon_g) + \alpha_g \left(C_{\epsilon 1} \frac{\epsilon_g}{k_g} P_k - C_{\epsilon 2} \rho_g \frac{\epsilon_g^2}{k_g} \right) + S_{\epsilon,d} \quad (15)$$

where

$$\mu_{eff,k,g} = \mu_{lam,g} + \frac{\mu_{turb(k-\epsilon),g}}{\sigma_k} \quad (16)$$

$$\mu_{eff,\epsilon,g} = \mu_{lam,g} + \frac{\mu_{turb(k-\epsilon),g}}{\sigma_\epsilon} \quad (17)$$

with the following model constants:

C_1	C_2	C_μ	σ_k	σ_w	Pr_t	Sc_t
1.44	1.92	0.09	0.90	1.30	0.85	0.7

The production of turbulent energy term is given as:

$$P_k = \vec{\tau}_g : \nabla \mathbf{v} \quad (18)$$

k-ω models

The k-ω model of Wilcox [6] is similar in structure to the k-ε model and is also based on the Boussinesq approximation. Two transport equations are solved to determine the two (large) scales of turbulence. The advantage of replacing the ε-equation by the ω-equation is that the second is easier to integrate (more robust), that it can be integrated through the sub-layer without the need for additional damping functions, and that it performs better for flows with weak adverse pressure gradient. The conservation equations are written as:

$$\frac{\partial}{\partial t}(\alpha_g \rho_g k_g) + \nabla \cdot (\alpha_g \rho_g \mathbf{v}_g k_g) = \nabla \cdot (\alpha_g \mu_{eff,k,g} \nabla k_g) + \alpha_g (P_k - \beta^* \rho_g k_g \omega_g) + S_{k,d} \quad (19)$$

$$\frac{\partial}{\partial t}(\alpha_g \rho_g \omega_g) + \nabla \cdot (\alpha_g \rho_g \mathbf{v}_g \omega_g) = \nabla \cdot (\alpha_g \mu_{eff, \omega, g} \nabla \omega_g) + \alpha_g \left(C_{\alpha 1} \frac{\omega_g}{k_g} P_k - C_{\beta 1} \rho_g \omega_g^2 \right) + S_{\omega, d} \quad (20)$$

with the following model constants:

$C_{\alpha 1}$	$C_{\beta 1}$	C_μ	β^*	σ_{k1}	$\sigma_{\omega 1}$	Pr_t	Sc_t
5/9	3/40	1	0.09	2	2	0.85	0.7

where

$$\mu_{turb(k-\omega), g} = \rho_g \frac{k}{\omega} \quad \mu_{eff, k, g} = \mu_{lam, g} + \frac{\mu_{turb(k-\omega), g}}{\sigma_{k1}} \quad \mu_{eff, \omega, g} = \mu_{lam, g} + \frac{\mu_{turb(k-\omega), g}}{\sigma_{\omega 1}} \quad (21)$$

The major drawback of the Wilcox model is that it is very sensitive to the values specified for ω in the free stream [20], which leads to strong dependence of the solution on the arbitrary specification of the free stream ω . This dependence is not present in the k- ϵ model.

The SST Model

In order to overcome the problem of free stream dependency in the Wilcox model, Menter [7] combined the two models so as to take advantage of their respective strength i.e. the robustness of the k- ω model near wall surfaces due to its simple low Reynolds number formulation and its ability to compute flows with weak adverse pressure gradients accurately, and the better performance of the k- ϵ model near the boundary layer edge and away from walls, due to its insensitivity to the free stream values. The basis of this technique is the transformation of the k- ϵ model to a k- ω formulation. This is an exact transformation, except for small contributions from the diffusion term due to the difference in the diffusion coefficients of the k and the ϵ equations. The k- ω formulation of the k- ϵ model is given by:

$$\frac{\partial}{\partial t}(\alpha_g \rho_g k_g) + \nabla \cdot (\alpha_g \rho_g \mathbf{v}_g k_g) = \nabla \cdot (\alpha_g \mu_{eff, k, g} \nabla k_g) + \alpha_g (P_k - \beta^* \rho_g k_g \omega_g) + S_{k, d} \quad (22)$$

$$\begin{aligned} \frac{\partial}{\partial t}(\alpha_g \rho_g \omega_g) + \nabla \cdot (\alpha_g \rho_g \mathbf{v}_g \omega_g) = & \nabla \cdot (\alpha_g \mu_{eff, \omega, g} \nabla \omega_g) \\ & + \alpha_g \left(C_{\alpha 2} \frac{\omega_g}{k_g} P_k - C_{\beta 2} \rho_g \omega_g^2 \right) + 2\sigma_{\omega 2} \frac{\rho}{\omega} \nabla k_g : \nabla \omega_g + S_{\omega, d} \end{aligned} \quad (23)$$

with the additional constants assigned the following values:

$C_{\alpha 2}$	$C_{\beta 2}$	σ_{k2}	$\sigma_{\omega 2}$
0.44	0.0828	1	0.856

The BSL model is derived by multiplying the k- ω equations (Eqs. (19),(20)) with a blending function F_1 and the k- ω formulated k- ϵ model equations (Eqs. (22),(23)) by $(1-F_1)$, yielding the following equations for k and ω [7]:

$$\frac{\partial}{\partial t}(\alpha_g \rho_g k_g) + \nabla \cdot (\alpha_g \rho_g \mathbf{v}_g k_g) = \nabla \cdot (\alpha_g \mu_{eff,k,g} \nabla k_g) + \alpha_g (P_k - \beta^* \rho_g k_g \omega_g) + S_{k,d} \quad (24)$$

$$\begin{aligned} \frac{\partial}{\partial t}(\alpha_g \rho_g \omega_g) + \nabla \cdot (\alpha_g \rho_g \mathbf{v}_g \omega_g) = & \nabla \cdot (\alpha_g \mu_{eff,\omega,g} \nabla \omega_g) \\ & + \alpha_g \left(\tilde{\alpha} \frac{\omega_g}{k_g} P_k - \tilde{\beta} \rho_g \omega_g^2 \right) + 2 \tilde{\sigma}_\omega \frac{\rho_g}{\omega_g} \nabla k_g : \nabla \omega_g (1 - F_1) + S_{\omega,d} \end{aligned} \quad (25)$$

This equation is formally very similar to that of the standard k- ω model, however all its coefficients depend on the blending function F_1 , in the form:

$$\tilde{\Phi} = F_1 \Phi_1 + (1 - F_1) \Phi_2 \quad (26)$$

The blending function F_1 depends on the solution variables and on the distance from the nearest wall and is given as:

$$F_1 = \tanh(\gamma_1^4) \quad (27)$$

where

$$\gamma_1 = \text{Min} \left(\text{Max} \left(\frac{\sqrt{k_g}}{\beta^* \omega_g y}, \frac{500\nu}{y^2 \omega_g} \right), \frac{4\rho \sigma_{\omega 2} k_g}{CD_{k\omega} y^2} \right) \quad (28)$$

and

$$CD_{k\omega} = \text{Max} \left(2\rho_g \sigma_{\omega 2} \frac{1}{\omega_g} \frac{\partial k_g}{\partial x_j} \frac{\partial \omega_g}{\partial x_j}, 10^{-10} \right) \quad (29)$$

The BSL model has a similar performance as the k- ω model for boundary layer flows and is nearly identical to the k- ϵ model for free shear flows. Its robustness is close to that of the k- ω model.

A further modification to the BSL model yields the SST [7] model which when compared to other eddy-viscosity models has an improved adverse pressure gradient performance. The modification is in the definition of the turbulent viscosity, which takes the form:

$$\mu_{turb,(SST),g} = \frac{\rho a_1 k_g}{\text{Max}(a_1 \omega_g, \Omega F_2)} \quad \mu_{eff,k,g} = \mu_{lam,g} + \frac{\mu_{turb,(SST),g}}{\tilde{\sigma}_k} \quad \mu_{eff,\omega,g} = \mu_{lam,g} + \frac{\mu_{turb,(SST),g}}{\tilde{\sigma}_\omega} \quad (30)$$

where Ω is the magnitude of the vorticity, and F_2 is given by [7]:

$$F_2 = \tanh(\gamma_2^2) \quad \text{with} \quad \gamma_2 = \text{Max} \left(2 \frac{\sqrt{k_g}}{\beta^* \omega_g y}, \frac{500\nu}{y^2 \omega_g} \right) \quad (31)$$

Conservation of Energy

The energy conservation equation is written using static enthalpy as the main variable:

$$\frac{\partial}{\partial t}(\alpha_g \rho_g h_g) + \nabla \cdot (\alpha_g \rho_g \mathbf{v}_g h_g) = -\nabla \cdot \dot{q}_g + \nabla \cdot \left(\frac{\mu_{turb,g}}{\text{Pr}_t} \nabla h_g \right) + S_{h,g} + \dot{M}_{vap,g} h_{vap,s} \quad (32)$$

with

$$\dot{q}_g = -\lambda_g \nabla T_g \quad (33)$$

In Eq.(33) λ is the thermal conductivity, and the gas enthalpy is defined as:

$$h_g = \sum_{k=(air,vap)} Y_k h_k = Y_{air,g} h_{air,g} + Y_{vap,g} h_{vap,g} \quad (34)$$

where

$$h_{air,g} = c_{p,air,g} (T_g - T^0) + h_{air,g}^0 \quad (35)$$

$$h_{vap,g} = c_{p,vap,g} (T_g - T_d) + c_{p,d} T_d + \Delta h(T_d) + h_{vap,g}^0$$

The $S_{h,g}$ term on the RHS of Eq. (32) is the source term due to gas-droplet interaction written as:

$$S_{h,g} = \pi D^2 \beta^* (T_d - T_g) \quad (36)$$

while in the last term:

$$h_{vap,g,s} = \Delta h_{vap}(T_d) + c_{p,d} T_d \quad (37)$$

with the subscript “s” being used to indicate that the enthalpy is evaluated at the droplet surface temperature, which in the case of the Uniform Temperature Model (adopted in this work) is equal to the droplet temperature T_d . Moreover, T^0 is the reference temperature, h^0 is the enthalpy of formation at the reference temperature, T_d is the droplet temperature (liquid state). Moreover, it is to be noted that the enthalpy of the vapor contains in addition to the enthalpy of formation a term known as the latent heat of vaporization, $\Delta h_{vap}(T_d)$, which accounts for the enthalpy absorbed during the phase change from liquid to vapor.

Conservation of Species

In Eq. (32), $Y_{vap,g}$ is the mass fraction of vapor in the gas phase and is obtained by solving the following mass fraction conservation equation:

$$\frac{\partial}{\partial t}(\alpha_g \rho_g Y_{vap,g}) + \nabla \cdot (\alpha_g \rho_g \mathbf{v}_g Y_{vap,g}) = \nabla \cdot (\alpha_g \Gamma_{Y_{vap,g}} \nabla Y_{vap,g}) + \alpha_g \rho_g \dot{Y}_{vap,g} \quad (38)$$

where

$$\Gamma_{Y_{vap,g}} = \Gamma_{Y_{vap,g}} + \frac{\mu_{turb,g}}{\sigma_{Y_{vap,g}}} \quad (39)$$

and $\sigma_{Y,g}$ is the turbulent Schmidt number of value 0.7 as given by Spalding [21]. Moreover, the source term on the RHS of equation (38) arises in the conversion of the species production rate to a concentration rate, as shown

$$\dot{Y}_{vap,g} = \frac{Y_{vap,g}(t + \Delta t) - Y_{vap,g}(t)}{\Delta t} \quad (40)$$

where

$$Y_{vap,g}(t) = \frac{m_{vap,g}}{m_{vap,g} + m_{air,g}} \quad (41)$$

$$Y_{vap,g}(t + \Delta t) = \frac{m_{vap,g} + \Delta m_{vap,g}}{m_{vap,g} + \Delta m_{vap,g} + m_{air,g}}$$

and

$$\frac{1}{\rho_g} = \frac{Y_{vap}}{\rho_{vap}} + \frac{Y_{air}}{\rho_{air}} \quad (42)$$

Substituting equation (41) into equation (40), we get:

$$\begin{aligned} \dot{Y}_{vap,g} &= \frac{\frac{m_{vap,g} + \Delta m_{vap,g}}{m_{vap,g} + m_{air,g} + \Delta m_{vap,g}} - \frac{m_{vap,g}}{m_{vap,g} + m_{air,g}}}{\Delta t} \\ &= \frac{\Delta m_{vap,g}}{\Delta t} \frac{m_{air,g}}{m_g(m_g + \Delta m_{vap,g})} = \frac{\dot{m}_{vap,g}}{m_g} Y_{air,g} \end{aligned} \quad (43)$$

or

$$\begin{aligned} \alpha_g \rho_g \dot{Y}_{vap,g} &= \alpha_g \frac{\rho_g}{m_g} \dot{m}_{vap,g} Y_{air,g} \\ &= \alpha_g \frac{\dot{m}_{vap,g}}{V_g} (1 - Y_{vap,g}) = \alpha_g \frac{\dot{m}_{vap,g}}{(\alpha_g V)} (1 - Y_{vap,g}) \\ &= \frac{\dot{m}_{vap,g}}{V} (1 - Y_{vap,g}) \\ &= \dot{M}_{vap,g} (1 - Y_{vap,g}) \end{aligned} \quad (44)$$

and equation (38) becomes

$$\frac{\partial}{\partial t} (\alpha_g \rho_g Y_{vap,g}) + \nabla \cdot (\alpha_g \rho_g \mathbf{v}_g Y_{vap,g}) = \nabla \cdot (\alpha_g \Gamma_{Y_{vap,g}, eff} \nabla Y_{vap,g}) + \dot{M}_{vap,g} (1 - Y_{vap,g}) \quad (45)$$

In the above equation $\dot{M}_{vap,g}$ was assumed to be known. An expression for $\dot{M}_{vap,g}$ ($\dot{M}_{vap,g} = -\dot{M}_d$), the volumetric mass rate of droplet evaporation, will be derived later.

DROPLET BALANCE EQUATION

Droplet evaporation is modeled by means of the Uniform Temperature Model [22,23]. This model is based on the assumption of a homogeneous internal temperature distribution in the droplet and phase equilibrium conditions at the surface. The analytical derivation of this model does not consider contributions to heat and mass transport through forced convection by the gas flow around the droplet. Since diffusive time scales in the surrounding gas phase are much smaller than that in the

droplet fluid, a quasi-stationary description of the gas phase is applied. The general assumptions for the model are:

1. The droplets are basically spherical
2. The exchange of mass, momentum and energy are quasi-steady
3. The transfer coefficients of mass, momentum and energy are expressed empirically, independent of the neighboring droplets.

Droplet Evaporation Sub-Model

Due to the difference in temperature and concentration between the surface of a liquid droplet and its surrounding gas, a droplet may eventually transform into the gas-phase. This process is called droplet evaporation. The evaporation of droplets is essentially a complex heat and mass transfer process. Heat transfer first raises the droplet's temperature until it reaches the wet bulb temperature. Then, all the heat transferred to the liquid is used in evaporation and the temperature of the rest of the liquid phase remains unchanged, this is what is known as the classical quasi-steady uniform temperature droplet model. The evaporation rate is commonly expressed as

$$\frac{dm_d}{dt} = \dot{m}_d^* \quad (46)$$

where m_d is the mass of the liquid droplet and, \dot{m}_d^* , the mass flux, corrected using the Frössling correlation and based on the classical droplet vaporization model [11,24]. Using reference values for variables fluid properties based on the 1/3 rule of Sparrow and Gregg [25], an integration of the radially symmetric differential equations yields and expression for the transport fluxes. The mass flux is given by:

$$\dot{m}_d^* = cfm \dot{m}_d = cfm \left[-2\pi D \hat{\rho}_g \hat{\Gamma}_g \ln \left(\frac{1 - Y_{vap,g}}{1 - Y_{vap,s}} \right) \right] \quad (47)$$

in this equation the $\hat{}$ indicate that the variable is evaluated at the reference temperature and mass fraction, defined as

$$\hat{T} = \frac{1}{3} T_{vap,g} + \frac{2}{3} T_{vap,s} \quad (48)$$

$$\hat{Y} = \frac{1}{3} Y_{vap,g} + \frac{2}{3} Y_{vap,s} \quad (49)$$

where $T_{vap,s}$ and $Y_{vap,s}$ are the temperature and mass fraction of the vapor at the surface of the droplet. Thus $\hat{\rho}_g$ and $\hat{\Gamma}_g$ are the density and diffusivity of the gas evaluated at the reference temperature and mass fraction.

In the Uniform Temperature Model, the temperature at the droplet surface is basically equal to that of the droplet:

$$T_{vap,s} = T_d \quad (50)$$

On the other hand, the vapor concentration on the surface of the droplet is found using the exponential law of Cox-Antoine [22], which states that:

$$X_{vap,s}(P_{sat}) = \frac{P_{sat}}{P} \quad (51)$$

with the saturation pressure P_{sat} for a droplet at temperature T_d obtained from:

$$P_{sat}(T_d) = e^{\left(A + \frac{B}{T_d + C}\right)} \quad (52)$$

where A, B and C are specific values for the droplet liquid under consideration. Thus

$$Y_{vap,s} = \frac{X_{vap,s} MW_{vapor}}{X_{vap,s} MW_{vapor} + (1 - X_{vap,s}) MW_{air}} \quad (53)$$

The liquid droplet takes its energy from the gas, which increases the liquid temperature. Once enough energy has been supplied to overcome the latent heat of evaporation, evaporation is initiated. This can be mathematically expressed as:

$$h_{vap,g,s} - h_{d,s} = \Delta h_{vapor}(T_{d,s}) \quad (54)$$

The equation for the heat transfer to the liquid droplet is given by:

$$m_d \frac{d(c_p T_d)}{dt} = \dot{H}_{evap,s} + \dot{Q}_{conv,s} \quad (55)$$

where h_d is the enthalpy of the liquid droplet, and $\dot{Q}_{conv,s}$ and $\dot{Q}_{evap,s}$ are the convection and evaporation heat transfer rates, respectively, written as:

$$\dot{Q}_{conv,s} = \pi D^2 \beta^* (T_{g,s} - T_d) \quad (56)$$

where β^* in equation (56) is the corrected convective heat transfer coefficient defined as:

$$\beta^* = cfh\beta = cfh \frac{-\frac{\dot{m}_d \hat{c}_{p,g}}{\pi D^2}}{\left(e^{\left(\frac{\dot{m}_d \hat{c}_{p,g}}{2\pi D \hat{\lambda}_g} \right)} - 1 \right)} \quad (57)$$

and

$$\dot{Q}_{evap,s} = \dot{m}_d^* \Delta h_v(T_{g,s}) \quad (58)$$

The correction factors cfm and cfh [11] account for convective mass and heat transport and are computed from:

$$cfm = 1 + 0.276 \text{Re}_d^{1/2} \text{Sc}_d^{1/3} \quad (59)$$

$$cfh = 1 + 0.276 \text{Re}_d^{1/2} \text{Pr}_d^{1/3} \quad (60)$$

where Re_d , Sc_d , and Pr_d are the Reynolds, Schmidt, and Prandtl numbers respectively, defined as:

$$\text{Re}_d = \frac{\rho_g \|\mathbf{v}_g - \mathbf{v}_d\| D_d}{\hat{\mu}_g} \quad (61)$$

$$\text{Sc}_d = \frac{\hat{\mu}_g}{\hat{\rho}_g \hat{\Gamma}_{dg}} \quad (62)$$

$$\text{Pr}_d = \frac{\hat{\mu}_g \hat{c}_{p,g}}{\hat{k}_g} \quad (63)$$

$\hat{\lambda}_g$ and $\hat{\Gamma}_{vap,g}$ are the conductivity and diffusivity of the water vapor evaluated at the reference temperature. The convection term in equation (55) represents the amount of energy due to the interaction between the droplet and gas phases, and is thus equal in magnitude to the $S_{h,g}$ term in the energy equation of the gas phase, that is:

$$S_{h,g} = \dot{Q}_{conv,s} \quad (64)$$

Note that the energy equation for the droplet can also be written as

$$\begin{aligned} \frac{d(m_d h_d)}{dt} &= m_d \frac{d(h_d)}{dt} + h_d \frac{d(m_d)}{dt} \\ &= \dot{m}_d \Delta h_v(T_{g,s}) + \pi D^2 \beta (T_{g,s} - T_g) + \dot{m}_d h_d \end{aligned} \quad (65)$$

in this case mass balance is accounted for in the energy balance.

Droplet Diameter Equation

A relation between the mass and the droplet diameter can be derived as follows. Starting with the mass of a droplet of volume V_d , we have:

$$m_d = \rho_d V_d = \rho_d \frac{\pi D^3}{6} \quad (66)$$

As the droplet vaporizes, the rate of mass decrease is:

$$\frac{dm_d}{dt} = \rho_d \frac{\pi D^2}{2} \frac{dD}{dt} \quad (67)$$

Finally before deriving the Eulerian formulation of the droplet mode, we define for later use the volumetric mass rate of droplet evaporation as

$$\dot{M}_d = \frac{m_d^*}{V} = \frac{m_d^*}{(V_d / \alpha_d)} = \frac{6\alpha_d}{\pi D^3} m_d^* \quad (68)$$

DROPLET DISCRETE LIQUID PHASE

The droplet liquid phase governing equations are derived by re-formulating the droplet Lagrangian model into the Eulerian framework. This is performed through the use of the material derivative.

Mass Conservation

In the Eulerian approach an additional continuity equation is needed for the droplet phase. For the mass conservation we have

$$\frac{\partial}{\partial t} (\alpha_d \rho_d) + \nabla \cdot (\alpha_d \mathbf{v}_d \rho_d) = \nabla \cdot \left(\frac{\mu_{turb,d}}{Sc_{turb,d}} \nabla \alpha_d \right) + \dot{M}_d \quad (69)$$

Again we have a term on the RHS, which is similar in form to diffusion but which really accounts for the dispersion of the droplet in the gas.

Momentum Conservation

In the Lagrangian approach, a momentum equation for every droplet is derived through a force balance and is given as:

$$\frac{D(\rho_d V_d \mathbf{v}_d)}{Dt} = -V_d \nabla P + \rho_d V_d \mathbf{g} + F^D + m_d^* \mathbf{v}_d \quad (70)$$

In the Eulerian approach the droplets are no longer tracked individually, but the ensemble average is used i.e. using the droplet (liquid) volume fraction:

$$\alpha_d = \frac{n V_d}{V} \quad (71)$$

When the Lagrangian equation is summed over all droplets and the volume fraction substituted, the Eulerian momentum equation for the droplet phase is found to be:

$$\frac{\partial}{\partial t} (\alpha_d \rho_d \mathbf{v}_d) + \nabla \cdot (\alpha_d \mathbf{v}_d \rho_d) = -\alpha_d \nabla P + \mathbf{F}^B + \mathbf{F}^D + \dot{M}_d \mathbf{v}_d \quad (72)$$

where

$$\mathbf{F}_d^D = -\mathbf{F}_g^D \quad (73)$$

$$\mathbf{F}_d^B = \alpha_d \rho_d \mathbf{g} \quad (74)$$

For turbulent flow, an extra term is added on the right hand side of Eq. (74), which should not be interpreted as a diffusion term since the droplets can be regarded as “solid particles” and thus non-diffusive entities. Instead, this term represents the dispersion of the droplets in the gas due to turbulent interaction, and this dispersion term have a similar form as the diffusion term in the momentum equation of the gas phase, thus the momentum equation for the droplet phase becomes:

$$\begin{aligned} \frac{\partial}{\partial t} (\alpha_d \rho_d \mathbf{v}_d) + \nabla \cdot (\alpha_d \mathbf{v}_d \rho_d) = & -\alpha_d \nabla P + \\ & \nabla \cdot (\alpha_d \mu_{turb,d} [\nabla \mathbf{v}_d + \nabla \mathbf{v}_d^T]) + \alpha_d \rho_d \mathbf{g} + \mathbf{F}^D + \dot{M}_d \mathbf{v}_d \end{aligned} \quad (75)$$

Droplet Diameter Equation

A relation between $\dot{M}_{vap,d}$ and $\dot{m}_{vap,d}$ can be readily derived, defining the volumetric mass rate as [22,26],

$$\begin{aligned} \dot{M}_d &= \frac{m_d^*}{V} = \frac{m_d^*}{(V_d / \alpha_d)} = \alpha_d \frac{6}{\pi D^3} m_d^* \\ &= \alpha_d \frac{6}{\pi D^3} \rho_d \frac{\pi D^2}{2} \frac{dD}{dt} \\ &= \rho_d \frac{3\alpha_d}{D} \frac{dD}{dt} \end{aligned} \quad (76)$$

Thus

$$\frac{dD}{dt} = \frac{D}{3\alpha_d \rho_d} \dot{M}_d \quad (77)$$

In order to derive the transport equation for the droplet diameter we first write

$$\nabla \cdot (\alpha_d \mathbf{v}_d \rho_d D) = D \nabla \cdot (\alpha_d \mathbf{v}_d \rho_d) + \alpha_d \mathbf{v}_d \rho_d \cdot \nabla D \quad (78)$$

noting that

$$\frac{dD}{dt} = \frac{\partial D}{\partial t} + \mathbf{v}_d \cdot \nabla D \quad (79)$$

we get:

$$\begin{aligned} \frac{\partial}{\partial t} (\alpha_d \rho_d D) + \nabla \cdot (\alpha_d \mathbf{v}_d \rho_d D) &= D \frac{\partial}{\partial t} (\alpha_d \rho_d) + (\alpha_d \rho_d) \frac{\partial D}{\partial t} + D \nabla \cdot (\alpha_d \mathbf{v}_d \rho_d) + \alpha_d \mathbf{v}_d \rho_d \cdot \nabla D \\ &= D \underbrace{\left(\frac{\partial}{\partial t} (\alpha_d \rho_d) + \nabla \cdot (\alpha_d \mathbf{v}_d \rho_d) \right)}_{\dot{M}_d + \nabla \cdot \left(\frac{\mu_{turb,d}}{Sc_{turb,d}} \nabla \alpha_d \right)} + \alpha_d \rho_d \underbrace{\left(\frac{\partial D}{\partial t} + \mathbf{v}_d \cdot \nabla D \right)}_{\frac{dD}{dt}} \\ &= 3\alpha_d \rho_d \frac{dD}{dt} + D \nabla \cdot \left(\frac{\mu_{turb,d}}{Sc_{turb,d}} \nabla \alpha_d \right) + \alpha_d \rho_d \frac{dD}{dt} \\ &= 4\alpha_d \rho_d \frac{dD}{dt} + D \nabla \cdot \left(\frac{\mu_{turb,d}}{Sc_{turb,d}} \nabla \alpha_d \right) \\ &= \frac{4}{3} D \dot{M}_d + D \nabla \cdot \left(\frac{\mu_{turb,d}}{Sc_{turb,d}} \nabla \alpha_d \right) \end{aligned} \quad (80)$$

To account for turbulence the above equation is written as:

$$\frac{\partial}{\partial t} (\alpha_d \rho_d D) + \nabla \cdot (\alpha_d \mathbf{v}_d \rho_d D) = \nabla \cdot \left(\alpha_d \frac{\mu_{turb,d}}{Pr_{turb,d}} \nabla D \right) + D \nabla \cdot \left(\frac{\mu_{turb,d}}{Sc_{turb,d}} \nabla \alpha_d \right) + \frac{4}{3} D \dot{M}_d \quad (81)$$

Energy Conservation

A transport equation for the droplet temperature can also be derived via an energy balance in the same manner as the momentum equation, this equation is written as:

$$\begin{aligned}
 \frac{\partial}{\partial t}(\alpha_d \rho_d h_d) + \nabla \cdot (\alpha_d \rho_d \mathbf{v}_d h_d) \\
 = h_d \frac{\partial}{\partial t}(\alpha_d \rho_d) + h_d \nabla \cdot (\alpha_d \rho_d \mathbf{v}_d) + \alpha_d \rho_d \frac{\partial}{\partial t}(h_d) + \alpha_d \rho_d \mathbf{v}_d \cdot \nabla(h_d) \\
 = \alpha_d \rho_d \underbrace{\left(\frac{\partial}{\partial t}(h_d) + \mathbf{v}_d \cdot \nabla(h_d) \right)}_{\frac{dh_d}{dt} = c_{p,d} \frac{dT_d}{dt}} + h_d \underbrace{\left(\frac{\partial}{\partial t}(\alpha_d \rho_d) + \nabla \cdot (\alpha_d \rho_d \mathbf{v}_d) \right)}_{\dot{M}_d + \nabla \cdot \left(\frac{\mu_{turb,d}}{Sc_{turb,d}} \nabla \alpha_d \right)}
 \end{aligned} \quad (82)$$

Following the derivation of Faeth [22] and Wittig [26] in relation to droplet heating and evaporation using the so called “Uniform Temperature Model”, the balance equations for the droplet mass and temperature are

$$\frac{dm_d}{dt} = -2\pi D \rho_{g,ref} \Gamma_{im,ref} \ln \left(\frac{1 - Y_{vap,g}}{1 - Y_{vap,s}} \right) cfm \quad (83)$$

$$\begin{aligned}
 c_{P,d} \frac{dT_d}{dt} &= -\frac{1}{m_d} \frac{dm_d}{dt} \left[\frac{cfh}{cfm} c_{P,vap,ref} (T_g - T_d) \left(\left[\frac{1 - Y_{vap,g}}{1 - Y_{vap,s}} \right]^{\frac{1}{Le}} - 1 \right)^{-1} - \Delta h_v \right] \\
 &= -\frac{1}{m_d} (-\dot{m}_{vap,d}) \left[\frac{cfh}{cfm} c_{P,vap,ref} (T_g - T_d) \left(\left[\frac{1 - Y_{vap,g}}{1 - Y_{vap,s}} \right]^{\frac{1}{Le}} - 1 \right)^{-1} - \Delta h_v \right] \\
 &= -\frac{1}{\rho_d v_d} (-\dot{m}_{vap,d}) \left[\frac{cfh}{cfm} c_{P,vap,ref} (T_g - T_d) \left(\left[\frac{1 - Y_{vap,g}}{1 - Y_{vap,s}} \right]^{\frac{1}{Le}} - 1 \right)^{-1} - \Delta h_v \right] \\
 &= \frac{6\dot{m}_{vap,d}}{\rho_d \pi D^3} \frac{cfh}{cfm} c_{P,vap,ref} (T_g - T_d) \left(\left[\frac{1 - Y_{vap,g}}{1 - Y_{vap,s}} \right]^{\frac{1}{Le}} - 1 \right)^{-1} - \frac{6\dot{m}_{vap,d}}{\rho_d \pi D^3} \Delta h_v \\
 &= \frac{\pi D^2}{\rho_d \alpha_d} \alpha^* (T_g - T_d) - \frac{\dot{M}_{vap,g}}{\rho_d \alpha_d} \Delta h_v = \frac{\pi D^2}{\rho_d \alpha_d} \alpha^* (T_g - T_d) + \frac{\dot{M}_d}{\rho_d \alpha_d} \Delta h_v
 \end{aligned} \quad (84)$$

where

$$\begin{aligned}
\alpha^* &= \frac{1}{\pi D^2} \frac{6\dot{m}_{vap,d}}{\rho_d \pi D^3} \frac{cfh}{c_{P,vap,ref}} \left(\left[\frac{1-Y_{vap,g}}{1-Y_{vap,s}} \right]^{\frac{1}{Le}} - 1 \right)^{-1} \rho_d \alpha_d \\
\dot{m}_{vap,d} &= 2\pi D \rho_{g,ref} \Gamma_{im,ref} \ln \left(\frac{1-Y_{vap,g}}{1-Y_{vap,s}} \right) c_{fm} \quad Le = \frac{\lambda_{g,ref}}{\rho_{g,ref} c_{P,vap,ref} \Gamma_{im,ref}} cfh = 1 + 0.276 \sqrt{\text{Re}_d} \text{Pr}^{1/3} \\
\alpha^* &= \rho_d \alpha_d \frac{\frac{1}{\pi D^2} \frac{6\dot{m}_{vap,d}}{\rho_d \pi D^3} \frac{cfh}{c_{P,vap,ref}}}{e^{\frac{1}{Le} \ln \left[\frac{1-Y_{vap,g}}{1-Y_{vap,s}} \right]} - 1} \\
&= \rho_d \alpha_d cfh \frac{\frac{1}{\rho_d \alpha_d} \frac{c_{P,vap,ref} \dot{M}_{vap,d}}{\pi D^2 c_{fm}}}{e^{\frac{\rho_{g,ref} c_{P,vap,ref} \Gamma_{im,ref}}{\lambda_{g,ref}} \frac{\dot{m}_{vap,d}}{2\pi D \rho_{g,ref} \Gamma_{im,ref} c_{fm}}} - 1} \\
&= cfh \frac{\frac{c_{P,vap,ref} \dot{M}_{vap,d}}{\pi D^2 c_{fm}}}{e^{\frac{\dot{m}_{vap,d} c_{P,vap,ref}}{2\pi D \lambda_{g,ref} c_{fm}}} - 1} = cfh \frac{\frac{c_{P,vap,ref} \dot{M}_d}{\pi D^2 c_{fm}}}{e^{\frac{\dot{m}_{vap,d} c_{P,vap,ref}}{2\pi D \lambda_{g,ref} c_{fm}}} - 1} \quad (85)
\end{aligned}$$

In the above equation the first term on the RHS accounts for heat exchange with the surrounding and the second term on the RHS accounts for the evaporation latent heat.

The energy equation is now rewritten as:

$$\frac{\partial}{\partial t} (\alpha_d \rho_d h_d) + \nabla \cdot (\alpha_d \rho_d \mathbf{v}_d h_d) = 2\pi D \beta (T_g - T_d) + \dot{M}_d (\Delta h_v + h_d) + h_d \nabla \cdot \left(\frac{\mu_{turb,d}}{Sc_{turb,d}} \nabla \alpha_d \right) \quad (86)$$

To account for turbulence the above equation is rewritten as:

$$\begin{aligned}
\frac{\partial}{\partial t} (\alpha_d \rho_d h_d) + \nabla \cdot (\alpha_d \rho_d \mathbf{v}_d h_d) &= \nabla \cdot \left(\alpha_d \frac{\mu_{turb,d}}{\text{Pr}_{turb,d}} \nabla h_d \right) + h_d \nabla \cdot \left(\frac{\mu_{turb,d}}{Sc_{turb,d}} \nabla \alpha_d \right) + \\
&\quad \pi D^2 \beta^* (T_g - T_d) + \dot{M}_d (\Delta h_v + h_d)
\end{aligned} \quad (87)$$

where $\mu_{turb,d}$ is the turbulent viscosity in the disperse phase computed using the algebraic model described next.

Turbulence Model in the Secondary Dispersed phase

Many workers [3,13,14] have successfully used the closure hypotheses for the turbulent mass, momentum, and heat transfer fluxes used in this work. Moreover, the turbulent viscosity of the disperse (droplet) phase, $\mu_{turb,d}$, is modeled using the approach of Melville and Bray [27]:

$$\mu_{turb,d} = \mu_{turb,g} \frac{\rho_d}{\rho_g} \frac{k_d}{k_g} \quad (88)$$

with

$$k_d = \frac{1}{2} \overline{\mathbf{v}'_d \cdot \mathbf{v}'_d} \quad (89)$$

A fundamental assumption of this approach is the dependence of the turbulent viscosity of the droplet phase on local mean flow properties. As for the ratio of the

turbulent kinetic energies of the dispersed and gas phase it is calculated following the approach of Krämer [28] as:

$$\frac{k_d}{k_g} = \frac{1}{1 + \omega^2 \tau^2} \quad (90)$$

where τ is the particle relaxation time, and ω is the frequency of the particle response which are given by:

$$\omega = \frac{1}{\tau} \left(\frac{\sqrt{\frac{2}{3}} k_g}{L_x} \tau \right)^{1/4} \quad (91)$$

$$\tau = \frac{1}{18} \frac{\rho_d}{\rho_g} \frac{D^2}{\nu} \frac{1}{1 + 0.133 \text{Re}_d^{0.687}}$$

with the following characteristic macroscopic length scale for turbulence

$$L_x = (c_\mu)^{3/4} \frac{(k_g)^{3/2}}{\epsilon_g} \quad (92)$$

Since in general the droplets do not follow the motion of the surrounding fluid from one point to another it is expected for the ratio k_d/k_g to be different from unity and to vary with particle relaxation time τ and local turbulence quantities. For the turbulent Schmidt number of the droplet phase, $Sc_{turb,d}$, Krämer [28] suggests a value of 0.3. However in more recent work [4] it was found to be particle size dependent and a value of 0.7 is used in this work ($Sc_{turb,d} = 0.7$). For the turbulent Prandtl number a value of 0.85 was chosen ($Pr_{turb,d} = 0.85$).

Numerical Approach

A review of the above differential equations reveals that they are similar in structure. If a typical representative variable associated with phase (k) is denoted by $\phi^{(k)}$, the general fluidic differential equation may be written as:

$$\frac{\partial(\alpha^{(k)} \rho^{(k)} \phi^{(k)})}{\partial t} + \nabla \cdot (\alpha^{(k)} \rho^{(k)} \mathbf{v}^{(k)} \phi^{(k)}) = \nabla \cdot (\alpha^{(k)} \Gamma^{(k)} \nabla \phi^{(k)}) + \alpha^{(k)} Q^{(k)} \quad (93)$$

where the expression for $\Gamma^{(k)}$ and $Q^{(k)}$ can be deduced from the parent equations.

DISCRETIZATION PROCEDURE

In the previous sections the differential equations governing multi-fluid flow phenomena of spray mixing and evaporation were outlined. The task now is to present the Finite Volume-based numerical solution algorithm for solving these equations.

Discretization of the general fluidic conservation equation

The general conservation equation (93) is integrated over a finite volume to yield:

$$\begin{aligned} \iint_{\Omega} \frac{\partial(\alpha^{(k)} \rho^{(k)} \phi^{(k)})}{\partial t} d\Omega + \iint_{\Omega} \nabla \cdot (\alpha^{(k)} \rho^{(k)} \mathbf{u}^{(k)} \phi^{(k)}) d\Omega \\ = \iint_{\Omega} \nabla \cdot (\alpha^{(k)} \Gamma^{(k)} \nabla \phi^{(k)}) d\Omega + \iint_{\Omega} \alpha^{(k)} Q^{(k)} d\Omega \end{aligned} \quad (94)$$

Where Ω is the volume of the control cell. Using the divergence theorem to transform the volume integral into a surface integral and then replacing the surface integral by a summation of the fluxes over the sides of the control volume, equation (91) is transformed to:

$$\frac{\partial(\alpha^{(k)} \rho^{(k)} \phi^{(k)} \Omega)}{\partial t} + \sum_{nb=e,w,n,s,t,b} (\mathbf{J}_{nb}^{(k)D} + \mathbf{J}_{nb}^{(k)C}) = \alpha^{(k)} Q^{(k)} \Omega \quad (95)$$

where $\mathbf{J}_{nb}^{(k)D}$ and $\mathbf{J}_{nb}^{(k)C}$ are the diffusive and convective fluxes, respectively. The discretized form of the diffusive flux along an east face is given by:

$$\mathbf{J}_e^{(k)D} = -\alpha_e^{(k)} \Gamma_e^{(k)} \left[(\phi_E^{(k)} - \phi_P^{(k)}) \frac{\mathbf{S}_e \mathbf{S}_e}{\mathbf{S}_e \mathbf{d}_e} + (\overline{\nabla \phi^{(k)}})_e \cdot \kappa_e \right] \quad (96)$$

where the over bar denotes a value obtained by interpolation, κ_e is a space vector defined as,

$$\kappa_e = (\hat{\mathbf{n}}_e - (\gamma \hat{\mathbf{d}})_e) \mathbf{S}_e = \kappa_e^x \mathbf{i} + \kappa_e^y \mathbf{j} + \kappa_e^z \mathbf{k} \quad (97)$$

and γ is a scaling factor given by [29],

$$\gamma_e = \frac{1}{\hat{\mathbf{n}}_e \cdot \hat{\mathbf{d}}_e} = \frac{\mathbf{S}_e \mathbf{d}_e}{\mathbf{S}_e \mathbf{d}_e} \quad (98)$$

and $\hat{\mathbf{n}}_f$ and $\hat{\mathbf{d}}_f$ are the contravariant and covariant unit vectors respectively. The discretized convective flux along an east face is given by:

$$\mathbf{J}_e^{(k)C} = (\alpha^{(k)} \rho^{(k)} \mathbf{u}^{(k)} \cdot \mathbf{S})_e \phi_e^{(k)} = (\alpha^{(k)} \rho^{(k)} U^{(k)})_e \phi_e^{(k)} = C_e^{(k)} \phi_e^{(k)} \quad (99)$$

where \mathbf{S}_e and C_e are the surface vector and convection flux coefficient at cell face 'e', respectively. As can be seen from Eq. (99), the accuracy of the control volume solution for the convective scalar flux depends on the proper estimation of the face value ϕ_e as a function of the neighboring ϕ nodes values. Using some assumed interpolation profile, ϕ_e can be explicitly formulated in terms of the nodal values by a functional relationship of the form:

$$\phi_e = f(\phi_{nb}) \quad (100)$$

where ϕ_{nb} denotes the ϕ values at the neighboring nodes. The interpolation profile may be one-dimensional or multi-dimensional of low or high order of accuracy. The higher the order of the profile is, the lower numerical diffusion will be. However, the order of the profile and its dimensionality do not eliminate numerical dispersion. To minimize this error, limiters on the convective flux should be imposed to enforce monotonicity [30]. For more details the reader is referred to [31].

After substituting the face values by their functional relationship relating to the node values of ϕ , Eq. (95) is transformed after some algebraic manipulations into the following discretized equation:

$$A_p^{(k)} \phi_p^{(k)} = \sum_{NB} A_{NB}^{(k)} \phi_{NB}^{(k)} + B_p^{(k)} \quad (101)$$

where the coefficients $A_p^{(k)}$ and $A_{NB}^{(k)}$ depend on the selected scheme and $B_p^{(k)}$ is the source term of the discretized equation. In compact form, the above equation can be written as

$$\phi_p^{(k)} = H_p [\phi^{(k)}] = \frac{\sum_{NB} A_{NB}^{(k)} \phi_{NB}^{(k)} + B_p^{(k)}}{A_p^{(k)}} \quad (102)$$

Discretization of the fluidic momentum equation

The discretization procedure for the momentum equation yields an algebraic equation of the form:

$$A_p^{(k)} \mathbf{u}_p^{(k)} = \sum_{NB(P)} A_{NB}^{(k)} \mathbf{u}_{NB}^{(k)} + \mathbf{B}_p^{(k)} - \alpha_p^{(k)} \Omega_p \nabla_p(P) + \Omega_p \sum_{m \neq k} g^{(km)} (\mathbf{u}_p^{(m)} - \mathbf{u}_p^{(k)}) \quad (103)$$

In the above equation, the inter-phase term is written out explicitly to show the strong coupling among the momentum equations of the different fluids. This is different from the *spatial* coupling that exists among the neighboring velocities of the same fluid. To improve the overall convergence and robustness of the algorithm, the inter-phase source term can be linearized and the linear part treated implicitly so that:

$$A_p^{(k)} \mathbf{u}_p^{(k)} = \sum_{NB} A_{NB}^{(k)} \mathbf{u}_{NB}^{(k)} + \mathbf{B}_p^{(k)} - \alpha_p^{(k)} \Omega_p \nabla_p(P) + \Omega_p \sum_{m \neq k} g^{(km)} \mathbf{u}_p^{(m)} \quad (104)$$

Where now

$$A_p^{(k)} \leftarrow A_p^{(k)} + \Omega_p \sum_{m \neq k} (g^{(km)}) \quad (105)$$

For later reference, the discretized form of the momentum equation is written in the following two forms:

$$\mathbf{u}_p^{(k)} = \mathbf{H} \mathbf{P}_p [\mathbf{u}^{(k)}] - \alpha^{(k)} \mathbf{D}_p^{(k)} \nabla_p(P) \quad (106)$$

where the body force and inter-phase terms are absorbed in the $\mathbf{B}_p^{(k)}$ source term within the $\mathbf{H} \mathbf{P}_p [\mathbf{u}^{(k)}]$ term, or as

$$\mathbf{u}_p^{(k)} = \mathbf{H} \mathbf{I}_p [\mathbf{u}^{(k)}] + \mathbf{D}_p^{(k)} \sum_{m \neq k} (g^{(km)} \mathbf{u}_p^{(m)}) \quad (107)$$

where the body force and pressure gradient terms are absorbed in the $\mathbf{B}_p^{(k)}$ source term within the $\mathbf{H} \mathbf{I}_p [\mathbf{u}^{(k)}]$ term.

Discretization of the fluidic mass conservation equation

The fluidic mass-conservation equation can be viewed as a fluidic volume fraction equation:

$$\alpha_p^{(k)} = H_p [\alpha^{(k)}] \quad (108)$$

or as a fluidic continuity equation to be used in deriving the pressure correction equation:

$$\frac{(\alpha_p^{(k)} \rho_p^{(k)}) - (\alpha_p^{(k)} \rho_p^{(k)})^{old}}{\delta t} \Omega + \Delta_p [\alpha^{(k)} \rho^{(k)} \mathbf{u}^{(k)} \cdot \mathbf{S}] = \dot{M}^{(k)} \quad (109)$$

where the Δ operator represents the following operation:

$$\Delta_p [\Theta] = \sum_{f=NB(P)} \Theta_f \quad (110)$$

Discretization of the fluidic energy equation

The discretization of the energy equation follows that of the general fluidic scalar equation. The only difference is the one pertaining to the discretization of the additional source terms. Since a control volume approach is followed, the integral of these sources over the control volume appears in the discretized equation. By using the divergence theorem, the volume integral is transformed into a surface integral and the resultant discretized expressions evaluated explicitly.

SOLUTION PROCEDURE

The number of equations describing an n-fluid flow situation is: n phasic momentum equations, n phasic volume fraction (or mass conservation) equations, a geometric conservation equation, and for the case of compressible flow additional n auxiliary pressure-density relations. Moreover, the variables involved are the n phasic velocity vectors, the n phasic volume fractions, the pressure field, and for a compressible flow an additional n unknown phasic density fields. In the current work, the n momentum equations are used to calculate the n velocity fields, n-1 volume fraction (mass conservation) equations are used to calculate n-1 volume fraction fields, and the last volume fraction field calculated using the geometric conservation equation

$$\alpha^{(n)} = 1 - \sum_{k \neq n} \alpha^{(k)} \quad (111)$$

The remaining volume fraction equation can be used to calculate the pressure field that is shared by all phases. However, instead of using this last volume fraction equation, in the class of Mass Conservation Based Algorithms (MCBA) the global conservation equation is employed, i.e. the sum of the individual mass conservation equations, to derive a pressure correction equation as outlined next.

The Pressure Correction Equation

To derive the pressure-correction equation, the mass conservation equations of the various phases are added to yield the global mass conservation equation given by:

$$\sum_k \left\{ \frac{(\alpha_p^{(k)} \rho_p^{(k)}) - (\alpha_p^{(k)} \rho_p^{(k)})^{old}}{\delta t} \Omega + \Delta_p (\alpha^{(k)} \rho_p^{(k)} \mathbf{u}^{(k)} \cdot \mathbf{S}) \right\} = \sum_k \dot{M}^{(k)} = 0 \quad (112)$$

In the predictor stage a guessed or an estimated pressure field from the previous iteration, denoted by P° , is substituted into the momentum equations. The resulting velocity fields denoted by $\mathbf{u}^{(k)*}$ which now satisfy the momentum equations will not, in general, satisfy the mass conservation equations. Thus, corrections are needed in order to yield velocity and pressure fields that satisfy both equations. Denoting the corrections for pressure, velocity, and density by P' , $\mathbf{u}^{(k)'}$, and $\rho^{(k)'}$ respectively, the corrected fields are written as:

$$P = P^\circ + P', \mathbf{u}^{(k)} = \mathbf{u}^{(k)*} + \mathbf{u}^{(k)'}, \rho^{(k)} = \rho^{(k)\circ} + \rho^{(k)'} \quad (113)$$

Hence the equations solved in the predictor stage are:

$$\mathbf{u}_p^{(k)*} = \mathbf{H}_p[\mathbf{u}^{(k)*}] - \alpha^{(k)\circ} \mathbf{D}_p^{(k)} \nabla_p P^\circ \quad (114)$$

While the final solutions satisfy

$$\mathbf{u}_p^{(k)} = \mathbf{H}_p[\mathbf{u}^{(k)}] - \alpha^{(k)} \mathbf{D}_p^{(k)} \nabla_p P \quad (115)$$

Subtracting the two equation sets ((115) and (114)) from each other yields the following equation involving the correction terms:

$$\mathbf{u}_p^{(k)} = \mathbf{H}_p[\mathbf{u}^{(k)}] - \alpha^{(k)\circ} \mathbf{D}_p^{(k)} \nabla_p P' \quad (116)$$

Moreover, the new density and velocity fields, $\rho^{(k)}$ and $\mathbf{u}^{(k)}$, will satisfy the overall mass conservation equation if:

$$\sum_k \left\{ \frac{(\alpha_p^{(k)\circ} \rho_p^{(k)}) - (\alpha_p^{(k)} \rho_p^{(k)})^{old}}{\delta t} \Omega + \Delta_p [\alpha^{(k)\circ} \rho^{(k)} \mathbf{u}^{(k)} \cdot \mathbf{S}] \right\} = 0 \quad (117)$$

Linearizing the $(\rho^{(k)} \mathbf{u}^{(k)})$ term, one gets

$$(\rho^{(k)*} + \rho^{(k)'}) (\mathbf{u}^{(k)*} + \mathbf{u}^{(k)'}) = \rho^{(k)*} \mathbf{u}^{(k)*} + \rho^{(k)*} \mathbf{u}^{(k)'} + \rho^{(k)'} \mathbf{u}^{(k)*} + \rho^{(k)'} \mathbf{u}^{(k)'} \quad (118)$$

Substituting equations (118) and (116) into equation (117), rearranging, and replacing density correction by pressure correction, the final form of the pressure-correction equation is written as:

$$\begin{aligned} \sum_k \left\{ \frac{\Omega}{\delta t} \alpha_p^{(k)\circ} C_\rho^{(k)} P'_p + \Delta_p [\alpha^{(k)\circ} U^{(k)*} C_\rho^{(k)} P'] - \Delta_p [\alpha^{(k)\circ} \rho^{(k)*} (\alpha^{(k)\circ} \mathbf{D}^{(k)} \nabla P') \cdot \mathbf{S}] \right\} \\ = - \sum_k \left\{ \frac{\alpha_p^{(k)\circ} \rho_p^{(k)*} - (\alpha_p^{(k)} \rho_p^{(k)})^{old}}{\delta t} \Omega + \Delta_p [\alpha^{(k)\circ} \rho^{(k)*} U^{(k)*}] \right\} \end{aligned} \quad (119)$$

The corrections are then applied to the velocity, pressure, and density fields using the following equations:

$$\mathbf{u}_p^{(k)*} = \mathbf{u}_p^{(k)\circ} - \alpha^{(k)\circ} \mathbf{D}_p^{(k)} \nabla_p P' \quad P^* = P^\circ + P' \quad \rho^{(k)*} = \rho^{(k)\circ} + C_\rho^{(k)} P' \quad (120)$$

Numerical experiments using the above approach to simulate air-water flows have shown poor conservation of the lighter fluid. This problem is considerably alleviated by normalizing the individual continuity equations, and hence the global mass conservation equation, by means of a weighting factor such as a reference density $\rho^{(k)}$

(which is fluid dependent). This approach has been adopted in solving all problems presented in this work (see [32] for details).

The MCBA-SIMPLE Algorithm

The overall solution procedure is an extension of the single-phase SIMPLE algorithm into multi-phase flows. Since the pressure correction equation is derived from overall mass conservation, it is denoted by MCBA-SIMPLE [31]. The sequence of events in the MCBA-SIMPLE is as follows:

1. Solve the fluidic momentum equations for velocities.
2. Solve the pressure correction equation based on global mass conservation.
3. Correct velocities, densities, and pressure.
4. Solve the fluidic mass conservation equations for volume fractions.
5. Solve the fluidic scalar equations (k , ϵ , T , Y , D , etc...).
6. Return to the first step and repeat until convergence.

Physical Properties

In the test problems that follow the material properties used for the water droplets, water vapor and air are as given by [33]:

$$\begin{aligned}
 MW_{air} &= 28.97 \text{ kg / kg mole} \\
 \mu_{air} &= 6.109 \times 10^{-6} + 4.604 \times 10^{-8} T - 1.051 \times 10^{-11} T^2 \text{ Kg / m.s} \\
 \lambda_{air} &= 3.227 \times 10^{-3} + 8.3894 \times 10^{-5} T - 1.9858 \times 10^{-8} T^2 \text{ J / m.s.K} \\
 Pr_{air} &= 0.815 - 4.958 \times 10^{-4} T + 4.514 \times 10^{-7} T^2 \text{ for } T \leq 600 \text{ K} \\
 Pr_{air} &= 0.647 + 5.5 \times 10^{-5} T \text{ for } T > 600 \text{ K} \\
 MW_{water} &= 18.015 \text{ kg / kg mole} \\
 c_{p,v} &= 8137 - 37.34xT + 0.07482xT^2 - 4.956 \times 10^{-5} T^3 \text{ J / kg.K} \\
 \mu_v &= 4.07 \times 10^{-8} T - 3.077 \times 10^{-6} \text{ Kg / m.s} \\
 \lambda_v &= 1.024 \times 10^{-2} - 8.21 \times 10^{-6} T + 1.41 \times 10^{-7} T^2 - 4.51 \times 10^{-11} T^3 \text{ J / m.s.K} \\
 \Delta h_v &= 2.257 \times 10^6 + 2.595 \times 10^3 (373.15 - T) \text{ J / kg} \\
 \rho_L &= 997 \text{ kg / m}^3 \\
 c_L &= 4184 \text{ J / kg.K} \\
 \lambda_L &= 0.6531 \text{ J / m.s.K}
 \end{aligned} \tag{121}$$

It is further assumed that the Lewis number is equal to unity and the diffusivity (Γ) is calculated with the density evaluated at the reference temperature.

The use of the above relations and materials are for convenience and should not be taken as restrictions related to the code.

Results and Discussion

In what follows, solutions to three two-dimensional two-phase flow problems are presented and discussed. The physical situations for these problems, depicted in Figs. 4(a)-4(c), represent a rectangular duct in which air enters with a uniform free stream velocity U , while fuel (water is used here) mixed with air is injected through a nozzle 2mm in diameter either in the stream-wise direction (Fig. 1(a)), or in the cross stream direction (Figs. 1(b) and 1(c)). The length of the domain is L ($L=1$ m) and its width is W ($W=0.25$ m). Turbulent flow results are generated using the k - ϵ , k - ω , and SST turbulence models. Moreover, the required temperature dependent properties of the carrier gas (air) and vapor species are as given above.

INJECTION IN THE STREAM-WISE DIRECTION

The physical domain depicted in Fig. 4(a) is subdivided into 120×89 non-uniform control volumes. The fuel is injected through 9 uniform control volumes (each of width $0.002/9$ m) with equal x-component of velocity ($=20\%$ of the free stream velocity) and different injection angles (varying uniformly from -45° to 45° as shown in Fig. 4(a)).

To validate the implemented evaporation model, the two-phase solution is compared against the single phase solution for the turbulent supersonic case ($M_{\text{inlet}}=2$) using the k - ϵ model. The single phase problem corresponds to exactly the same two-phase problem but with the injected water-air mixture replaced by air. Results generated are displayed in Fig. 5. In these plots, cross-stream profiles for the x-component of the gas velocity (Fig. 5(a)), the gas temperature (Fig. 5(b)), the gas density (Fig. 5(c)), and the gas turbulent kinetic energy (Fig. 5(d)) at three axial stations are compared. As depicted in Fig. 5(a), the two-phase U-velocity profiles indicate lower values than the single phase profiles, which is physically expected as the presence of particles injected at lower velocity than the gas phase creates drag that slows down the gas phase. In Fig. 5(b), the lower temperature values of the two-phase flow are also in accord with what is expected since the droplet phase absorbs heat as it evaporates and thereby decreases the temperature of the gas phase. Moreover, the higher density in the presence of droplets (Fig. 5(c)) is due to the water evaporating into air. As shown, the difference increases with distance as the mass fraction of water vapor increases. The turbulent kinetic energy profiles displayed in Fig. 5(d) indicate higher turbulence level in the presence of droplets, which is physically correct.

The size of the grid used in the computations to obtain grid independent solutions was selected after comparing results generated on grids of increasing density. As mentioned above, a final grid of size 121×91 grid points was chosen as results generated with this grid are almost identical to the ones generated using a grid of size 162×111 grid points. This is clearly seen in Fig. 6 where cross-stream profiles of the x-component of the gas velocity (Fig. 6(a)), gas temperature (Fig. 6(b)), vapor mass fraction in the gas phase (Fig. 6(c)), and droplet temperature (Fig. 6(d)) at three axial stations are compared.

Having established physical and numerical credibility, the problem is solved, as described next, for subsonic and supersonic conditions.

Subsonic evaporation and mixing of water droplets in air

For the physical situation depicted in Fig. 4(a), the Mach number and temperature of the air at inlet to the domain are taken to be 0.2 ($M_{air,inlet}=0.2$) and 900 K, respectively. The mixture of air and droplet are injected into the domain with a temperature of 300 K with the volume fraction of the water in the injected air-water mixture being 10^{-2} . The velocity of the injected mixture is given as (there is no particular reason for the choice of this velocity profile):

$$\begin{cases} \mathbf{v}_{d,injected} = 0.2 * \|\mathbf{v}\|_{g,inlet} \mathbf{i} + 0.2 * \|\mathbf{v}\|_{g,inlet} \sin\left(\frac{\pi}{4} - \frac{k-1}{4} \frac{\pi}{4}\right) \mathbf{j} & 1 \leq k \leq 9 \\ \mathbf{v}_{g,injected} = 0.3 * \|\mathbf{v}\|_{g,inlet} \mathbf{i} + 0.3 * \|\mathbf{v}\|_{g,inlet} \sin\left(\frac{\pi}{4} - \frac{k-1}{4} \frac{\pi}{4}\right) \mathbf{j} & 1 \leq k \leq 9 \end{cases} \quad (122)$$

With this injection velocity profile, there is a slip between the two injected phases and the magnitude of the injected velocity increases away from the center of the jet. Moreover, with this velocity profile and volume fraction a total of 0.479Kg/s of fuel are injected into the domain, which corresponds to an overall fuel-air ratio of 0.04124 kg_{fuel}/kg_{air}. This fuel/air ratio is at the high side of typical values used in gas turbine applications.

The problem is first solved assuming the flow to be laminar and then turbulent using the k-ε model and results are displayed in Figs. 7-9. In Fig. 7, contour plots for the laminar case are presented. In Figs. 7(a) and 7 (b) the droplet velocities and volume fraction fields are depicted. As shown, due to the higher air velocity, the spreading of injected water is low and droplets quickly align with the air velocity. As expected, the gas temperature (Fig. 7(c)) decreases along the centerline of the domain because of the droplet evaporation. This decrease in temperature is associated with an increase in density. The distribution of water vapor in the gas phase is displayed in Fig. 7(d) while the pressure field is depicted in Fig. 7(e). The mass fraction of the water vapor in the gas phase increases as the mixture moves downstream in the channel due to the increase in the evaporated amount with distance, which is physically plausible. Computations have shown that 26.953% of the water droplets entering the domain are transformed into water vapor.

Turbulent flow results for the same configuration and physical properties using the k-ε turbulence model are displayed in Fig. 8. Due to the higher mixing in turbulent flows, the droplets align faster with the gas field resulting in less spreading of the droplets in comparison with the laminar case, as depicted by the droplet velocity and volume fraction fields presented in Figs. 8(a) and 8(b). For the same reason, a higher decrease in temperature is obtained along the central portion of the domain (Fig. 8(c)) where the water vapor is concentrated (Fig. 8(d)). Unlike the laminar case, the pressure decreases in the stream-wise direction (Fig. 8(e)). To be mentioned is the fact that 26.947% of the water droplets entering the domain are transformed into water vapor. This is 0.06% lower than the value obtained in the laminar case and can be explained as follows: The two factors controlling the rate of evaporation are the residence time and rate of mixing. As the rate of increase in the x-component of the droplet velocity is lower for laminar flow than for turbulent flow (due to the lower mixing rate), the residence time

is higher for laminar than for turbulent flows. Consequently, in the laminar case, evaporation occurs over a longer period. However, this increase in residence time is associated with lower mixing and heat transfer rates, which is exactly opposite to what takes place in the turbulent case. These two competing and opposite effects seem to balance each other and tend to keep the rate of evaporation nearly the same for laminar and turbulent flows, even though the profiles of the various fields are different.

The decrease in the droplet diameter and increase in droplet temperature along the centerline of the channel is depicted in Fig. 9 for the turbulent flow case. As shown, the rate of increase in temperature is high in the early part of the channel where 90% of the total increase occurs over almost 25% of the channel length due to the relatively low gas velocity. This increase in temperature is associated with a local decrease in the rate of evaporation, which explains the slight decrease in the rate at which the diameter decreases.

Supersonic evaporation and mixing of water droplets in air

For the same physical situation depicted in Fig. 4, the air Mach number at inlet to the domain which is set to 2 ($M_{\text{air,inlet}}=2$) while the values of all other parameters are the same as in the subsonic case. Results are presented in Figs. 10-14. In Fig. 10, generated results for the laminar case are displayed. Similar results for turbulent flow using the $k-\epsilon$, $k-\omega$, and SST models are depicted in Fig. 11, 12, and 13, respectively. In all Figures, field plots of particle velocity (Figs. 11(a),12(a), and 13(a)), particle volume fraction (Figs. 11(b),12(b), and 13(b)), gas temperature (Figs. 11(c),12(c), and 13(c)), mass fraction of water vapor in the gas phase (Figs. 11(d),12(d), and 13(d)), and pressure (Figs. 11(e),12(e), and 13(e)) are presented. Due to their high inertia and the much lower viscous effects in the laminar flow case, the droplets are less affected by the gas and require a longer distance to align with the primary gas flow in comparison with the turbulent flow cases (compare the particle velocity fields in Figs. 10(a)-13(a)). In this case, the two forces other than inertia are the pressure gradient and drag. This explains the completely different pressure field obtained in the laminar case (Fig. 10(e)) as compared to pressure fields obtained with the various turbulence models (Figs. 11(e)-13(e)). Moreover, the general trend in variation of other variables is similar and resembles the subsonic case, i.e. the volume fraction of the particles decreases in the stream-wise direction, the gas temperature decreases along the central portion of the domain due to the absorption of heat by the droplets to evaporate, and the stream-wise increase in the mass fraction of the water vapor in the gas phase as more water evaporates.

To be noticed here are the droplet velocity profiles predicted by the various turbulence models displayed in Figs. 11(a)-13(a). The highest spreading is obtained with the $k-\epsilon$ model and the lowest spreading by the $k-\omega$ model. The predictions of the $k-\omega$ model, unlike the $k-\epsilon$ model, are well known to depend on the free stream values. It seems that the inlet turbulence quantities used in the simulation do not work well with the $k-\omega$ model. The inlet turbulence intensity is taken to be $I=5\%$ and the turbulence length scale $L=0.25$ (the height of the domain) and k , ϵ , and ω at inlet are computed as:

$$\left\{ \begin{array}{l} k_{g,inlet} = 1.5 * \left(\frac{I}{100} \right)^2 \mathbf{v}_{g,inlet} \cdot \mathbf{v}_{g,inlet} \\ \varepsilon_{g,inlet} = \frac{C_{\mu}^{0.75} (k)^{1.5}}{L} \\ \omega_{g,inlet} = \frac{\varepsilon_{g,inlet}}{C_{\mu} k} \end{array} \right. \quad (123)$$

In fact, by setting the value of ω at inlet to be equal to that of ε , spreading close to the one obtained in the laminar case was predicted. Therefore to be able to reproduce the k- ε predictions, the value of ω at inlet has to be adjusted through trial and error. This task has not been undertaken due to time limitation. The SST model is supposed to possess the virtues of both the k- ε model away from walls and the virtues of the k- ω model close to the wall and by including the cross diffusion terms, it becomes free-stream independent. Moreover, its predictions are expected to lie between those of the k- ε and k- ω models. As expected, results presented in Fig. 13 possess these properties. In fact, the highest turbulent viscosity over the domain, based on the above inlet turbulence quantities, is close to 4 Kg/(m.s) for the k- ε model, close to 28 Kg/(m.s) for the k- ω model, and close to 6 Kg/(m.s) for the SST model. Clearly, the higher the turbulent viscosity is, the less spreading is predicted.

The increase in the droplet temperature and decrease in the droplet diameter along the centerline of the channel, as predicted with the k- ε model, is depicted in Fig. 14. Due to the high speed of the flow, the droplet temperature does not reach its limiting wet bulb value. Moreover, the decrease in the droplet diameter is lower than in the subsonic case. In fact, computations have shown that only around 4.9% of the water droplets entering the domain are transformed into water vapor.

To study the effect of the various parameters on the evaporation rate, the SST model is selected and results are presented in Figs. 15-17. The effect of the inlet gas temperature is presented in Fig. 15. For that purpose, all parameters are held constants with the exception of the inlet gas temperature, which is varied between 300 and 1100 K. As expected, the rate of evaporation increases with increasing $T_{g,inlet}$. The highest value achieved is around 5.5%, which is still low and clearly demonstrates the difficulties one encounters in high speed flows. The effect of the droplet temperature on the rate of evaporation is displayed in Fig. 16. As shown, the $T_{d,inlet}$ is varied between 300 and 370 K, while holding all other parameters constants. The highest value used is slightly less than the water boiling temperature at normal atmospheric pressure. As depicted in Fig. 16, the rate of evaporation increases with increasing the droplet temperature. It can also be inferred from the figure that it is more advantageous to increase the droplet temperature than the gas temperature, as the highest rate of evaporation achieved with an inlet droplet temperature of 370 K is close to 14.4%. Finally, the effect of the domain length on the rate of evaporation is studied and results reported in Fig. 17. For that purpose, a droplet temperature of 370 K is selected and the length of the domain varied from 0.5 to 2 m and computations performed holding all other parameters constants. As expected, the rate of evaporation increases with increasing the domain length and for the longest domain its value is close to 20.5%.

INJECTION AT RIGHT ANGLE FROM ONE NOZZLE

The physical situation for this problem, depicted in Fig. 4(b), represents a rectangular duct in which air enters with a uniform free stream velocity U , while fuel (water is used here) mixed with air is injected from a nozzle on the lower horizontal wall of the domain. The length of the domain is L ($L=1$ m) and its width is W ($W=0.25$ m). Moreover, the required temperature dependent properties of the carrier gas (air) and vapor species are given by Eq.(121).

The Mach number and temperature of the air at inlet to the domain are taken to be 2 ($M_{\text{air,inlet}}=2$) and 900 K, respectively. The mixture of air and droplet enters the domain with a temperature of 300 K with the volume fraction of the water in the injected air-water mixture being 10^{-2} , the velocity of the fuel-air mixture is 10% the gas velocity in the main gas stream, with a fuel mass flow rate of 2.398 Kg/s. An 81x41 grid system is used and the fuel-air mixture is injected normal to the main gas stream from a nozzle 2mm in size using five control volumes. Moreover, results are generated for laminar and turbulent flow using the $k-\epsilon$, $k-\omega$, and SST turbulence models.

Results for this problem are presented in Figs. 18-22. Laminar flow plots are displayed in Fig. 18 whereas results for turbulent flow are presented in Figs. 19-21. The higher jet penetration experienced by the laminar computations as compared to the turbulent ones can be explained as follows. As shown in Figs. 18(a)-21(a), the highest turbulence of the gas phase is at inlet and decreases downstream due to its interaction with the normal jet that results in large dissipation, which is manifested by the increase in temperature near the nozzle inlet. Furthermore, the increased mixing in the turbulent simulation means that a higher percentage of the droplets have evaporated in the near nozzle zone and a lower momentum is available for the droplet to penetrate the gas stream. These results are consistent for all three turbulence models, with the $k-\epsilon$ model yielding slightly higher spreading than the other two models. This effect does point out to the importance that a turbulent gas phase can have on the injected fuel. The general trend of results is also consistent with the parallel test problem where the effects of the gas phase on the droplets being larger in turbulent rather than laminar flow. Nevertheless, the injected air-water droplet mixture is deflected by the free stream due to its high velocity ($M_{\text{inlet}}=2$). This is further reflected by the volume fraction fields (Figs. 18(b)-21(b)). As shown, the droplets carried by the high velocity stream, spread as they move towards the domain outlet. The gas temperature (Fig. 18(c)-21(c)) increases in the region around the injector due to the large decrease in velocity of the gas phase. This sudden decrease is supposed to be associated with a shock wave. Evidence of this shock wave can be noticed from the pressure contours (Figs. 18(e)-21(e)), which also shows the reflection of this wave after hitting the opposite wall. In fact the Mach number in the region around the inlet decreases to very low values. It is suspected that smearing of this shock wave is caused by numerical diffusion, which is a characteristic of the upwind scheme. Unfortunately, it has not been possible so far to obtain a converged solution using any of the high resolution schemes; this is expected to be resolved with more numerical experimentation. However for development purposes, it was deemed sufficient to obtain results with a first order scheme. Future developments will address this numerical issue. The predictions are physically sound and reveal a decrease in temperature due to evaporation in regions where droplets exist (Fig. 18(c)-21(c)) and an increase in the

mass fraction of the water vapor in the gas phase (Fig. 18(d)-21(d)) with increasing distance from the injector.

The increase in the droplet temperature and decrease in the droplet diameter along the centerline of the channel, as predicted with the k- ϵ model, are depicted in Fig. 22. It should be mentioned here that droplets are injected 10 cm from the channel inlet. Due to the high speed of the flow, the droplet temperature does not reach its limiting wet bulb value. Moreover, computations show that only about 5% of the water droplets entering the domain are transformed into water vapor due to the high velocities involved and consequently the short residence time of water droplets.

INJECTION AT RIGHT ANGLE FROM TWO OPPOSING NOZZLES

The physical situations for this problem, depicted in Figs. 4(c), is similar to that of the previous one, however water is injected from two nozzles on the lower and upper horizontal walls. Again the length of the domain is L ($L=1$ m) and its width is W ($W=0.25$ m). Moreover, the required temperature dependent properties of the carrier gas (air) and vapor species are given by Eq.(121).

The Mach number and temperature of the air at inlet to the domain are taken to be 2 ($M_{\text{air,inlet}}=2$) and 900 K, respectively. The mixture of air and droplet enters the domain with a temperature of 300 °K with the volume fraction of the water in the injected air-water mixture being 5×10^{-3} , the velocity of the fuel-air mixture is 10% the gas velocity in the main gas stream, with a fuel mass flow rate of 2.398 Kg/s. An 81x41 grid system is used and, as in the previous case, the fuel-air mixture is injected vertically upward through a 2mm nozzle (subdivided into 5 control volumes) along the lower horizontal wall and vertically downward through another 2mm nozzle (also subdivided into 5 control volumes) along the upper horizontal wall, with the two jets directly facing each others. Again, results are generated for laminar and turbulent flow using the k- ϵ , k- ω , and SST turbulence models and are displayed in Figs. 23-27.

Results follow the same trend noticed earlier. The droplet velocity Figs. 23(a)-26(a) and volume fraction fields depicted in Figs. 23(b)-26(b) reveal that both air-water droplet jets are deflected by the free stream and interact downstream towards the exit from the channel, with the two streams merging into one in the laminar case only (Fig. 23(a)) due to the reasons stated above. The gas temperature increases in the region around the injectors due to the formation of two shock waves which are smeared by the numerical diffusion, and then decreases in the area behind the shocks due to the heat absorbed for evaporation (Fig. 23(c)-26(c)). Moreover, viscous dissipation results in higher temperatures in the vicinity of the walls. The water vapor mass fraction increases as the mixture moves downstream in the channel (Figs. 23(d)-26(d)) due to the increase in the evaporated amount with distance. Pressure contours depicted in Figs. 23(e)-26(e) reflect the formation of the two oblique shock waves that are reflected back and forth along the upper and lower walls. Since these shock waves move in opposite direction they result in the presented pressure map.

The increase in the droplet temperature and decrease in the droplet diameter along the centerline of the channel, as predicted with the k- ϵ model, are depicted in Fig. 27. Again it should be mentioned that droplets are injected 10 cm from the channel inlet.

Closing Remarks

An Eulerian model involving discrete and continuous phases for the simulation of droplet evaporation and mixing at all speed was formulated and implemented. The model allows for continuous droplet size changes without recourse to a stochastic approach. The numerical procedures are based on a pressure-based multi-fluid finite volume method and form a solid base for the future inclusion of combustion and other modes of interactions such as droplet coagulation and break-up. In addition to the k - ϵ and k - ω turbulence models, the more recent SST model was also implemented for the continuous gas phase with a coupled algebraic model for the discrete phase. All models were appropriately modified to account for gas compressibility at high speeds. The code was tested by solving for evaporation and mixing in three very tough configurations, in the various Mach number regimes, and over a wide range of operating conditions for both laminar and turbulent flows. Even though water droplets were selected for the liquid phase, and only a two-component gas phase was used, this is not a code or a model limitation. The model can be used with more complex liquid fuels, and the code can handle multi-component multi-fluid flows, and as such set the stage for the simulation of scramjet combustion.

References

1. Kay, I.W., Peshke, W. T., and Guile, R. N., "Hydrocarbon-Fueled Scramjet Combustor Investigation," *Journal of Propulsion and Power*, March-April, 1992.
2. Burger, M., Klose, G., Rottenkolber, G., Schmehl, R., Giebert, D., Schafer, O., Koch, R., and Wittig, S., "A combined Eulerian and Lagrangian Method for Prediction of Evaporating Sprays," Proceedings of DETC'01, 2001 ASME Design Engineering Technical Conferences, June 4-7, 2001, New Orleans, Louisiana, USA.
3. Hallman M. Scheurlen M., Wittig S. "Computation of Turbulent Evaporating Sprays: Eulerian versus Lagrangian Approach," Transaction of the ASME, vol. 117, pp.112-119, 1995.
4. Wittig, S., Hallmann, M., Scheirlen, M., and Schmehl, R., "A new Eulerian model for turbulent evaporating sprays in recirculating flows," AGARD Meeting on "Fuel Combustion Technology for advanced Aircraft Engines", May 1993.
5. Launder, B.E. and Spalding, D.B., "The Numerical Computation of Turbulent Flows," *Comp. Methods Appl. Mech. Eng.*, vol. 3, pp. 269-289, 1974.
6. Wilcox D.C. "Turbulence Modeling for CFD", DCW Industries Inc., 1993.
7. Menter F.R. "Two-equation eddy-viscosity turbulence models for engineering applications", *AIAA Journal*, vol. 32, no 8, pp. 269-289, 1994.
8. Hassanizadeh M., Gray W.G. "General Conservation Equations for multi-phase systems, I Averaging procedure", *Adv. Water Resources*, vol. 2, pp. 131-190, 1979
9. Hassanizadeh M., Gray W.G., "General Conservation Equations for Multi-Phase Systems: 2, Mass, Momenta, Energy and Entropy Equations", *Adv. Water Res.*, vol. 2, pp. 191-202, 1979.
10. Launder B.E., Sharma B.I. "Application of the energy dissipation model of turbulence to the calculation of the flow near a spinning disk", *Letters in Heat and Mass Transfer*, vol. 1, no. 2, 1974.
11. Frössling N, "Über die Verdunstung fallender Tropfen", *Gerlands Beiträge zur Geophysik*, vol. 52, pp. 170-215, 1938.
12. Wiegand H., "Die Einwirkung eines ebene Stömungsfeldes auf frei bewegliche Tropfen und ihren Widerstandsbeiwert im Reynoldszahlenbereich von 50 bis 2000. Fortschrittberichte VDI, Reihe, 7, Nr 120, 1987.
13. Chen, C.P. and Wood, P.E., "Turbulence closure modeling of two-phase flows," *chemical Engineering Communications*, vol. 29, pp. 291-310, 1984.
14. Elgobashi, S.E., Abou-Arab, T.W., Rizk, M., and Moustafa, A., "Prediction of Particle Laden Jet with a Two-Equation Turbulence Model," *International Journal*

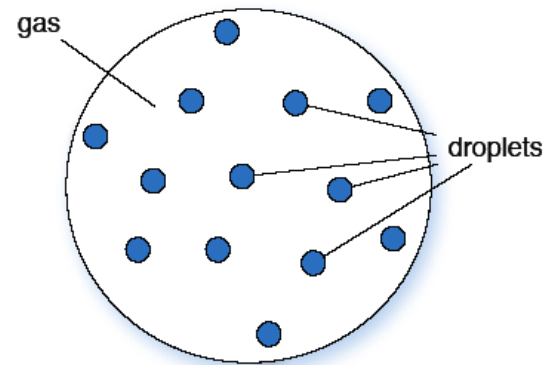
- of Multiphase Flow”, vol. 10, no. 6, pp. 697-710, 1984.
15. Pourahmadi, F. and Humphrey, J.A.C.,”Modeling solid-fluid turbulent flows with application to predicting erosive wear,” *Int. J. Phys. Chem. Hydro*, vol. 4, pp. 191-219, 1983.
 16. Lopez de Bertodano, M., Lee, S.J., Lahey, R.T. Jr., and Drew, D.A.,”The prediction of two-phase turbulence and phase distribution phenomena using a Reynolds stress model,” *ASME Journal of Fluids Engineering*, vo. 112, pp. 107-113, 1990.
 17. Lopez de Bertodano, M., Lahey, R.T. Jr., and Jones, O.C.,”Development of a k- ϵ model for bubbly two-phase flow,” *ASME Journal of Fluids Engineering*, vo. 116, pp. 128-134, 1994.
 18. Lopez de Bertodano, M., Lahey, R.T. Jr., and Jones, O.C.,” Phase distribution in bubbly two-phase flow in vertical ducts,” *Int. J. Multiphase flow*, vol. 20, no. 5, pp. 805-818, 1994.
 19. Cokljat, D., Ivanov, V.A., Srasola, F.J., and Vasquez, S.A.,”Multiphase K-Epsilon Models for Unstructured Meshes,” *ASME 2000 Fluids Engineering Division Summer Meeting*, June 11-15, 2000, Boston Massachusetts, USA.
 20. Menter F.R. “Influence of freestream values on k-w turbulence model predictions”, *AIAA Journal*, vol 30, no 6, pp. 1657-1659, 1992.
 21. Spalding D.B., “Concentration fluctuations in a round turbulent free jet”, *Chem. Engng. Sci.*, vol. 25, pp. 95-107, 1971.
 22. Faeth G.M., “Evaporation and Combustion of Sprays”, *Prog. Energy Combust. Sci.*, vol. 9, pp. 1-76, 1983
 23. Aggarwal S.K., Peng F., “A Review of Droplet Dynamics and Vaporization Modeling for Engineering Calculations”, *Trans. ASME: J. Eng. Gas Turb. Power*, vol. 117, pp. 453-461, 1995.
 24. Abramzon B., Sirignano W.A. “Droplet Vaporization Models for Spray Combustion Calculations”, *Int. J. Heat Mass Trans.*, vol. 32, pp.1605-1618, 1989.
 25. Sparrow F.M., Gregg J.L., “The variable fluid Property problem in Free Convection”, *transaction of ASME*, vol. 80, pp. 879-886, 1958.
 26. Wittig S., Klausmann W., Noll B., Himmelsbach J., “Evaporation of Fuel Droplets in turbulent Combustor Flow”, *ASME paper 88-GT-107*, 1988.
 27. Melville, W.K. and Bray, K.N.C, “A model of the two phase turbulent Jet,” *International Journal of Heat and Mass Transfer*, vol. 22, pp. 647-656, 1979.
 28. Krämer, M., Untersuchungen zum Bewegungsverhalten von Tropfen in turbulenter Strömung im Hinblick auf Verbrennungsvorgänge, Dissertation, Institut für Feuerungstechnik, Universität Karlsruhe (T.H.), 1988.

29. Zwart, P.J., Raithby, G.D., and Raw, M.J., "An integrated Space-Time Finite-Volume Method for Moving-Boundary Problems," *Numerical Heat Transfer Part B*, vol. 34, pp. 257-270, 1998.
30. Gaskell, P.H. and Lau, A.K.C., "Curvature compensated Convective Transport: SMART, a new boundedness preserving transport algorithm," *Int. J. Num. Meth. Fluids*, vol. 8, pp. 617-641, 1988.
31. Darwish, M.s. and Moukalled, F., "Normalized Variable and Space Formulation Methodology For High-Resolution Schemes," *Numerical Heat Transfer, Part B*, vol. 26, pp. 79-96, 1994.
32. Darwish, M., Moukalled, F., and, Sekar, B., "A Unified Formulation of the Segregated Class of Algorithms for Multi-Fluid Flow at All Speeds," *Numerical Heat Transfer, Part B: Fundamentals*, vol. 40, no. 2, pp. 99-137, 2001.
33. Harpole, G.M., "Droplet Evaporation in High Temperature Environment," *Journal of Heat Transfer*, vol. 103, pp. 86-91, 1981.

Figure Captions

- Fig. 1 Inter-penetrating media.
- Fig. 2 Terminology of the phase interface: A small area of the evaporative surface.
- Fig. 3 Uniform Droplet Temperature Model.
- Fig. 4 Physical domains.
- Fig. 5 Comparison of the single-phase and two-phase flow (a) U gas velocity, (b) gas temperature, (c) gas density, and (d) gas turbulent kinetic energy profiles at three axial stations generated using 109x160 control volumes.
- Fig. 6 Comparison of the (a) gas velocity, (b) gas temperature, (c) vapor mass fraction, and (d) droplet temperature profiles at three axial stations generated using 109x160 and 89x120 control volumes.
- Fig. 7 (a) droplet velocity, (b) droplet volume fraction, (c) gas temperature, (d) mass fraction of water vapor, and (e) pressure distribution over the domain (laminar flow, $M_{in}=0.2$, $T_{gas,in}=900$ K, $T_{d,in}=300$ K, and $\alpha_d=0.01$).
- Fig. 8 (a) droplet velocity, (b) droplet volume fraction, (c) gas temperature, (d) mass fraction of water vapor, and (e) pressure distribution over the domain (turbulent flow, k- ϵ model, $M_{in}=0.2$, $T_{gas,in}=900$ K, $T_{d,in}=300$ K, and $\alpha_d=0.01$).
- Fig. 9 Variation of droplet temperature and diameter along the center line of the domain (turbulent flow, k- ϵ model, $M_{in}=0.2$, $T_{gas,in}=900$ K, $T_{d,in}=300$ K, and $\alpha_d=0.01$).
- Fig.10 (a) droplet velocity, (b) droplet volume fraction, (c) gas temperature, (d) mass fraction of water vapor, and (e) pressure distribution over the domain (laminar flow, $M_{in}=2$, $T_{gas,in}=900$ K, $T_{d,in}=300$ K, and $\alpha_d=0.01$).
- Fig. 11 (a) droplet velocity, (b) droplet volume fraction, (c) gas temperature, (d) mass fraction of water vapor, and (e) pressure distribution over the domain (turbulent flow, k- ϵ model, $M_{in}=2$, $T_{gas,in}=900$ K, $T_{d,in}=300$ K, and $\alpha_d=0.01$).
- Fig. 12 (a) droplet velocity, (b) droplet volume fraction, (c) gas temperature, (d) mass fraction of water vapor, and (e) pressure distribution over the domain (turbulent flow, k- ω model, $M_{in}=2$, $T_{gas,in}=900$ K, $T_{d,in}=300$ K, and $\alpha_d=0.01$).
- Fig. 13 (a) droplet velocity, (b) droplet volume fraction, (c) gas temperature, (d) mass fraction of water vapor, and (e) pressure distribution over the domain (turbulent flow, SST model, $M_{in}=2$, $T_{gas,in}=900$ K, $T_{d,in}=300$ K, and $\alpha_d=0.01$).
- Fig. 14 Variation of droplet temperature and diameter along the center line of the domain (turbulent flow, k- ϵ model, $M_{in}=2$, $T_{gas,in}=900$ K, $T_{d,in}=300$ K, and $\alpha_d=0.01$).
- Fig. 15 The percentage, by mass, of the injected liquid droplets that evaporates at different inlet gas temperatures(turbulent flow, SST model, $M_{in}=2$, $T_{d,in}=300$ K, and $\alpha_d=0.01$).

- Fig. 16 The percentage, by mass, of the injected liquid droplets that evaporates at different inlet droplet temperature (turbulent flow, SST model, $M_{in}=2$, $T_{gas,in}=900$ K, and $\alpha_d=0.01$).
- Fig. 17 The percentage, by mass, of the injected liquid droplets that evaporates for different domain length (turbulent flow, k- ϵ model, $M_{in}=2$, $T_{gas,in}=900$ K, $T_{d,in}=370$ K, and $\alpha_d=0.01$).
- Fig. 18 (a) droplet velocity, (b) droplet volume fraction, (c) gas temperature, (d) mass fraction of water vapor, and (e) pressure distribution over the domain (laminar $M_{in}=2$, $T_{gas,in}=900$ K, $T_{d,in}=300$ K, and $\alpha_d=0.01$).
- Fig. 19 (a) droplet velocity, (b) droplet volume fraction, (c) gas temperature, (d) mass fraction of water vapor, and (e) pressure distribution over the domain (turbulent flow, k- ϵ model, $M_{in}=2$, $T_{gas,in}=900$ K, $T_{d,in}=300$ K, and $\alpha_d=0.01$).
- Fig. 20 (a) droplet velocity, (b) droplet volume fraction, (c) gas temperature, (d) mass fraction of water vapor, and (e) pressure distribution over the domain (turbulent flow, k- ω model, $M_{in}=2$, $T_{gas,in}=900$ K, $T_{d,in}=300$ K, and $\alpha_d=0.01$).
- Fig. 21 (a) droplet velocity, (b) droplet volume fraction, (c) gas temperature, (d) mass fraction of water vapor, and (e) pressure distribution over the domain (turbulent flow, SST model, $M_{in}=2$, $T_{gas,in}=900$ K, $T_{d,in}=300$ K, and $\alpha_d=0.01$).
- Fig. 22 Variation of droplet temperature and diameter along the center line of the domain (turbulent flow, k- ϵ model, $M_{in}=2$, $T_{gas,in}=900$ K, $T_{d,in}=300$ K, and $\alpha_d=0.01$).
- Fig. 23 (a) droplet velocity, (b) droplet volume fraction, (c) gas temperature, (d) mass fraction of water vapor, and (e) pressure distribution over the domain (laminar, $M_{in}=2$, $T_{gas,in}=900$ K, $T_{d,in}=300$ K, and $\alpha_d=0.005$).
- Fig. 24 (a) droplet velocity, (b) droplet volume fraction, (c) gas temperature, (d) mass fraction of water vapor, and (e) pressure distribution over the domain (turbulent flow, k- ϵ model, $M_{in}=2$, $T_{gas,in}=900$ K, $T_{d,in}=300$ K, and $\alpha_d=0.005$).
- Fig. 25 (a) droplet velocity, (b) droplet volume fraction, (c) gas temperature, (d) mass fraction of water vapor, and (e) pressure distribution over the domain (turbulent flow, k- ω model, $M_{in}=2$, $T_{gas,in}=900$ K, $T_{d,in}=300$ K, and $\alpha_d=0.005$).
- Fig. 26 (a) droplet velocity, (b) droplet volume fraction, (c) gas temperature, (d) mass fraction of water vapor, and (e) pressure distribution over the domain (turbulent flow, SST model, $M_{in}=2$, $T_{gas,in}=900$ K, $T_{d,in}=300$ K, and $\alpha_d=0.005$).
- Fig. 27 Variation of droplet temperature and diameter along the center line of the lower half of the domain (turbulent flow, k- ϵ model, $M_{in}=2$, $T_{gas,in}=900$ K, $T_{d,in}=300$ K, and $\alpha_d=0.005$).



V_g = volume of gas phase
 V_d = volume of droplet phase
 $V = V_g + V_d$ = total volume
 $\alpha_d = V_d/V$

Figure 1: interpenetrating media

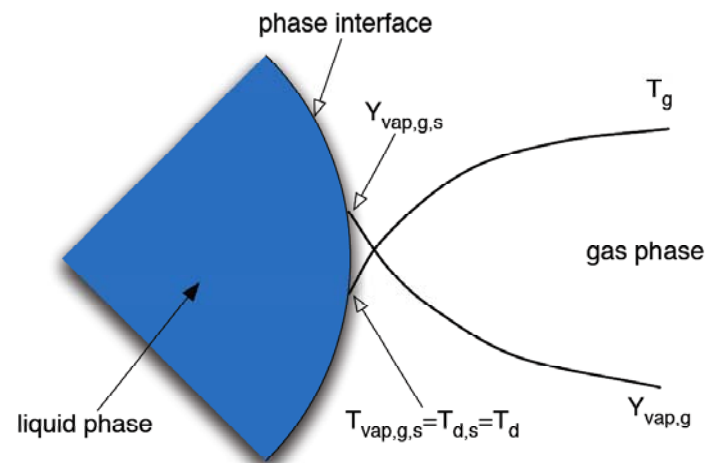


Figure 2: Terminology of the phase interface

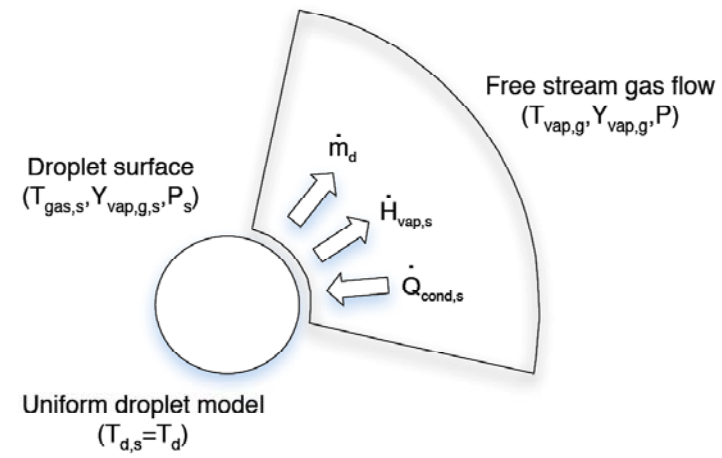


Figure 3: Uniform Droplet Temperature Model.

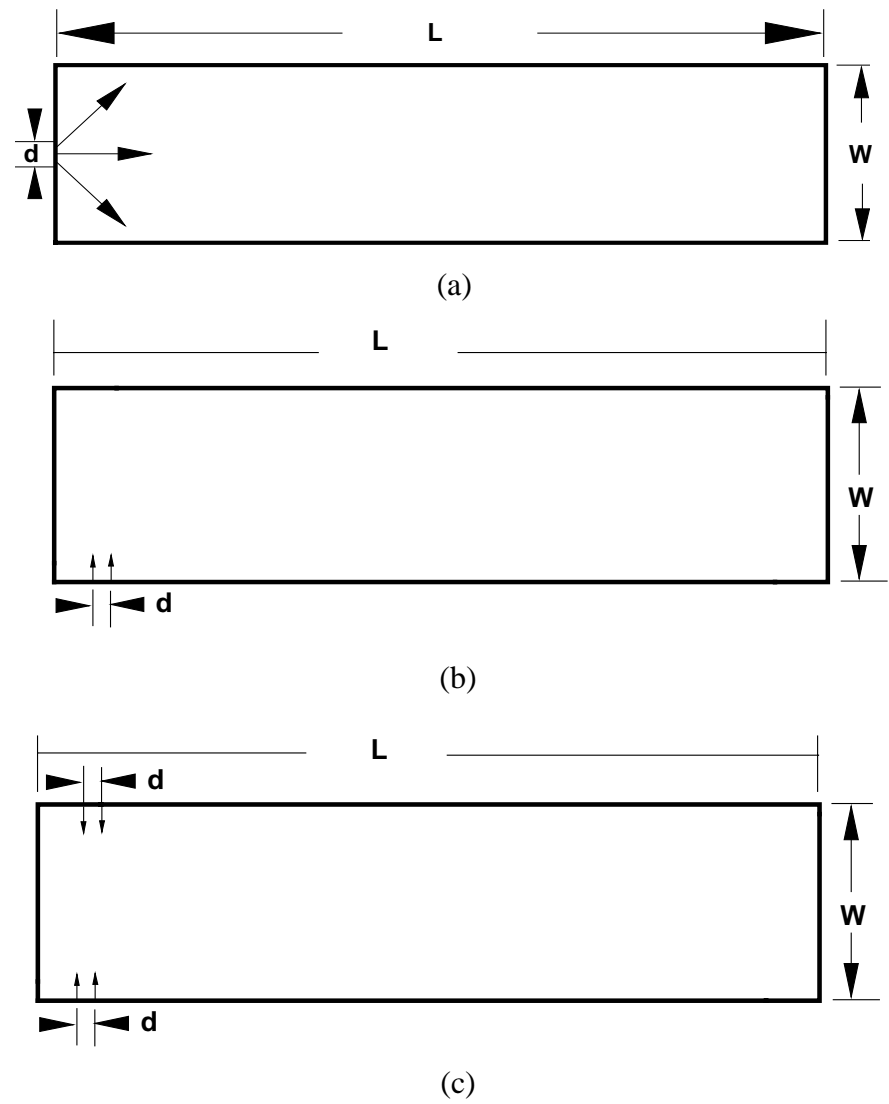
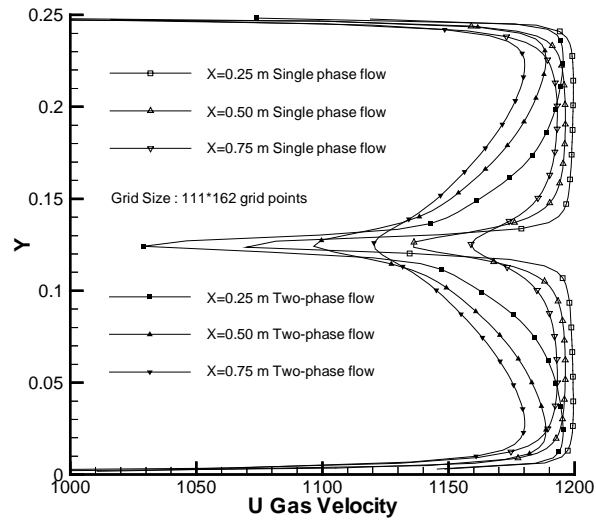
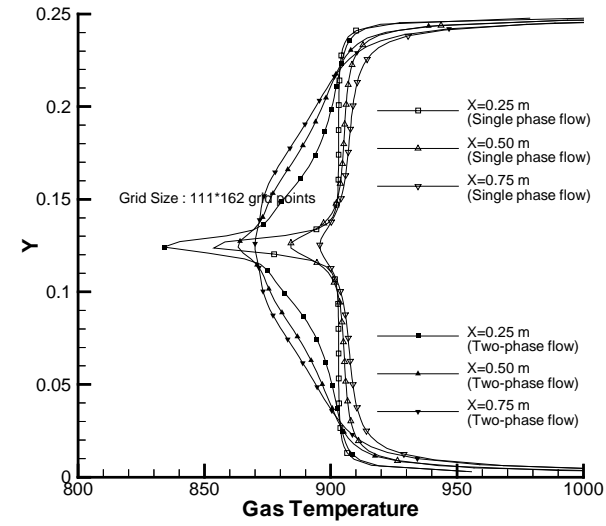


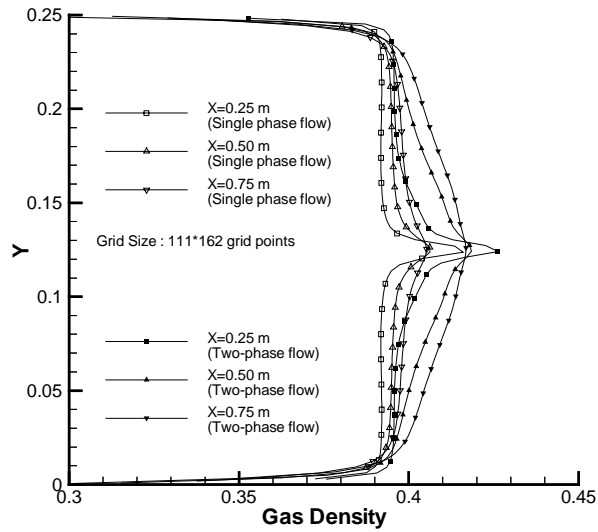
Fig. 4 Physical Situation



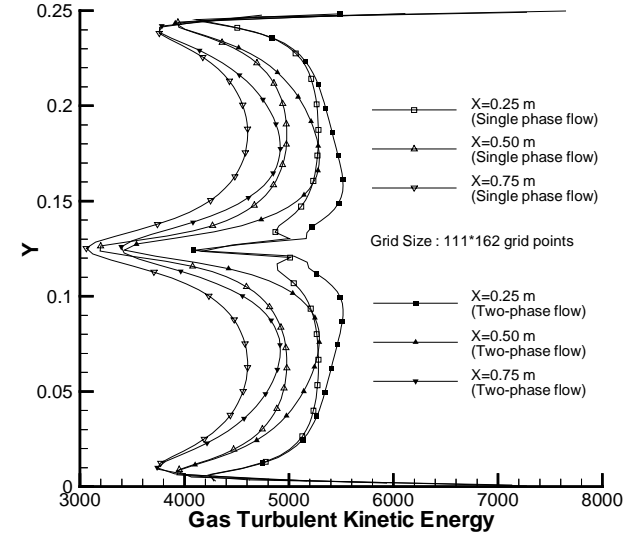
(a)



(b)



(c)



(d)

Figure 5 Comparison of the single-phase and two-phase flow (a) U gas velocity, (b) gas temperature, (c) gas density, and (d) gas turbulent kinetic energy profiles at three axial stations generated using 109x160 control volumes.

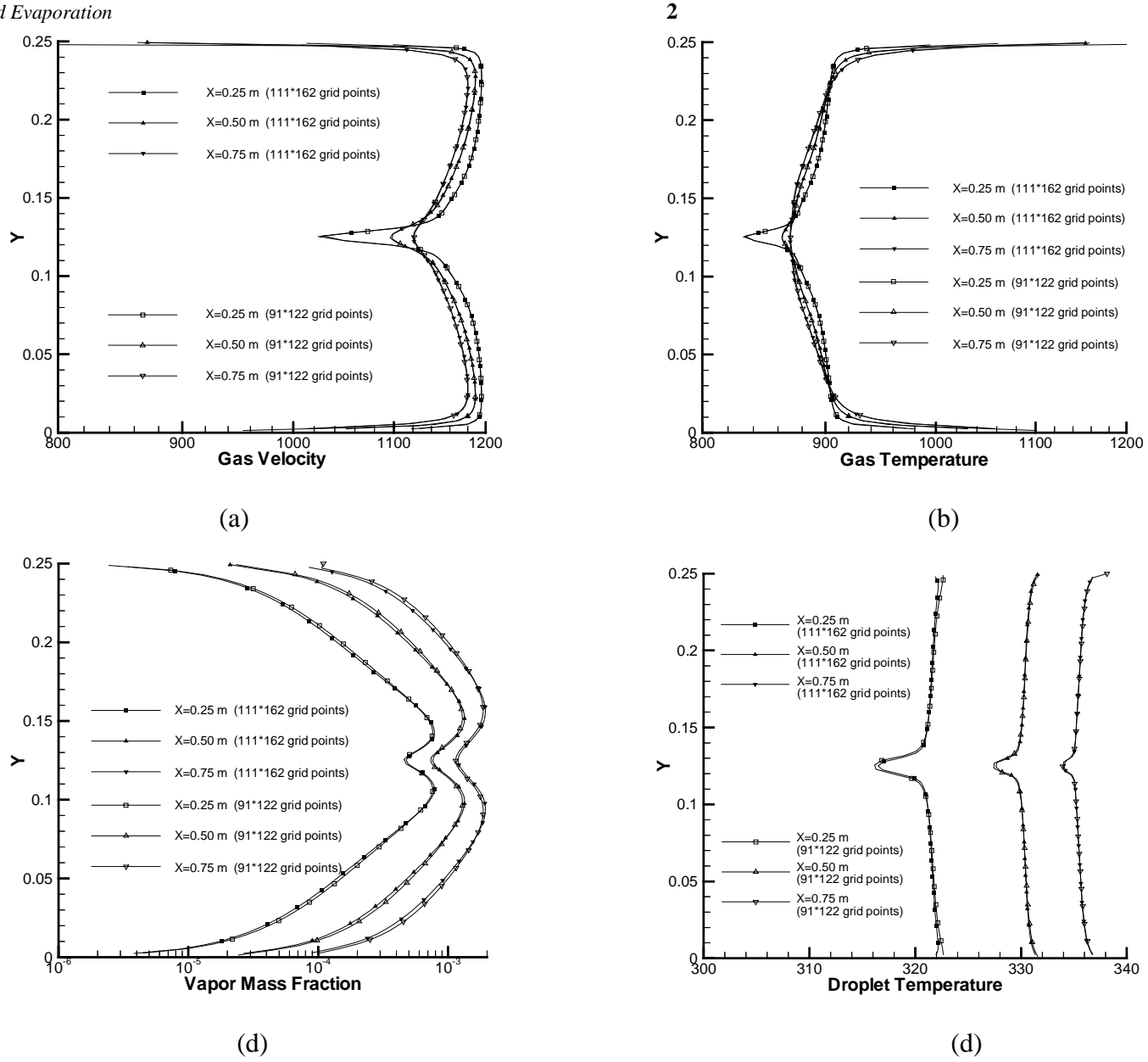


Figure 6 Comparison of the (a) gas velocity, (b) gas temperature, (c) vapor mass fraction, and (d) droplet temperature profiles at three axial stations generated using 109x160 and 89x120 control volumes.

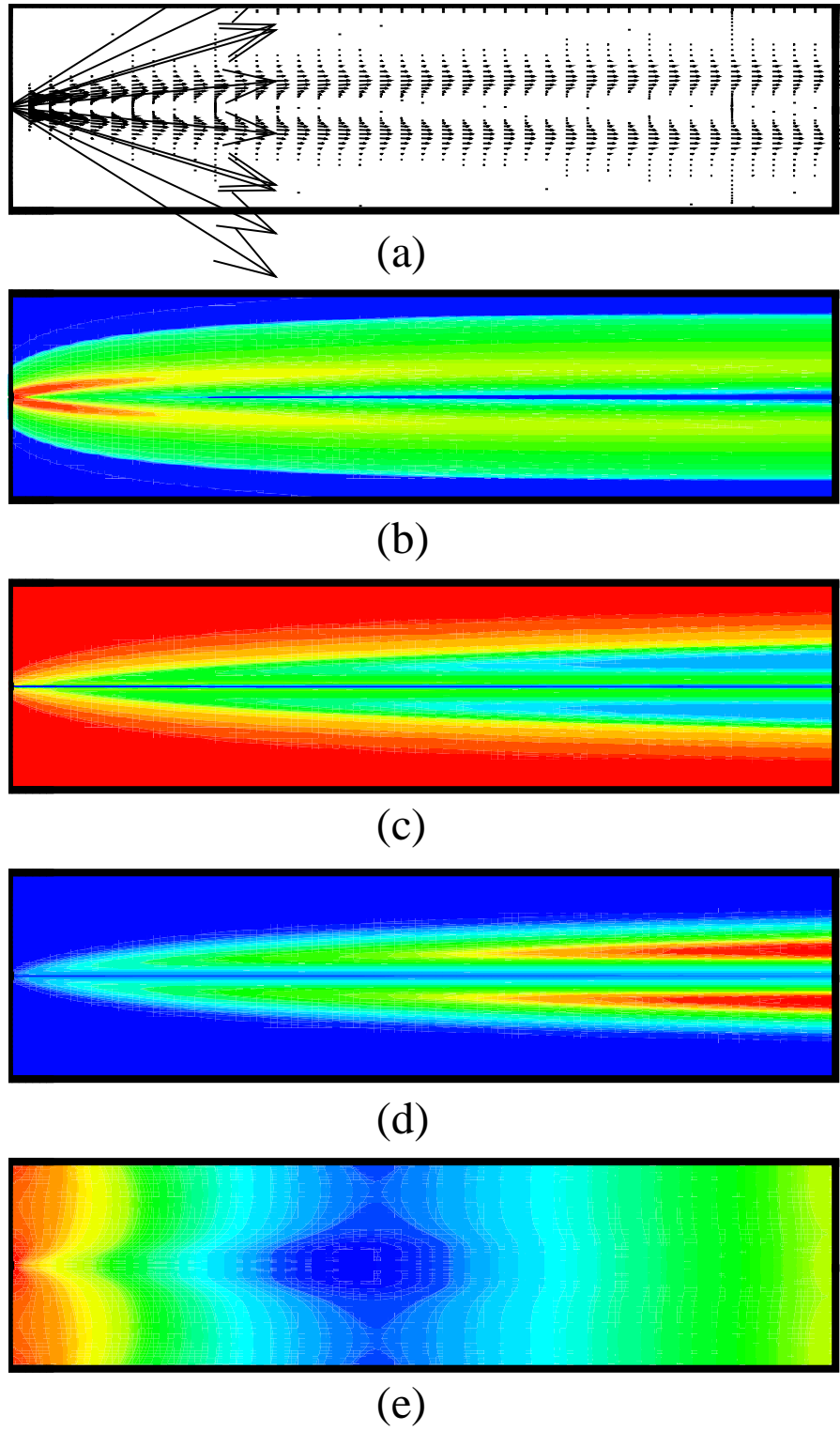


Fig. 7 (a) droplet velocity, (b) droplet volume fraction, (c) gas temperature, (d) mass fraction of water vapor, and (e) pressure distribution over the domain (laminar flow, $M_{in}=0.2$, $T_{gas,in}=900$ K, $T_{d,in}=300$ K, and $\alpha_d=0.01$).

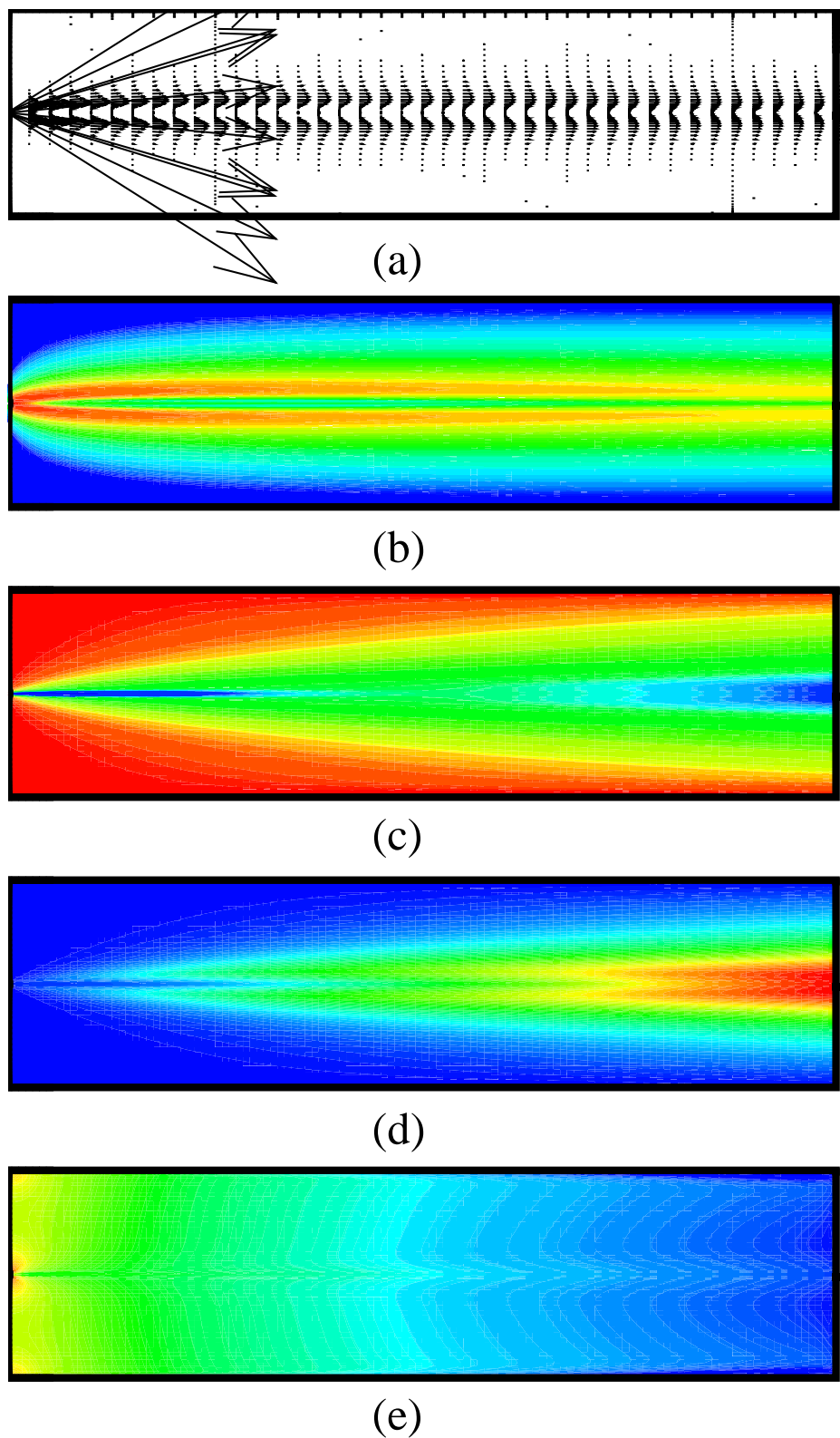


Fig. 8 (a) droplet velocity, (b) droplet volume fraction, (c) gas temperature, (d) mass fraction of water vapor, and (e) pressure distribution over the domain (turbulent flow, k- ϵ model, $M_{in}=0.2$, $T_{gas,in}=900$ K, $T_{d,in}=300$ K, and $\alpha_d=0.01$).

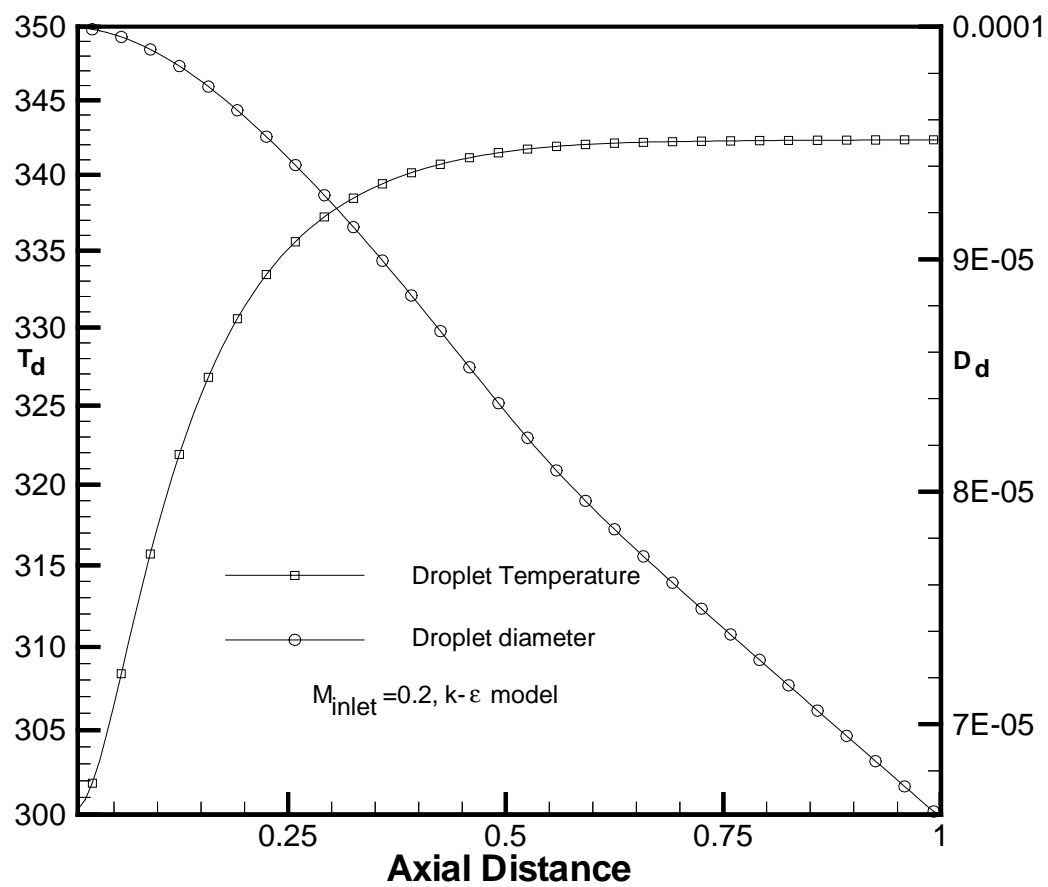


Fig. 9 Variation of droplet temperature and diameter along the center line of the domain (turbulent flow, k- ϵ model, $M_{in}=0.2$, $T_{gas,in}=900$ K, $T_{d,in}=300$ K, and $\alpha_d=0.01$).

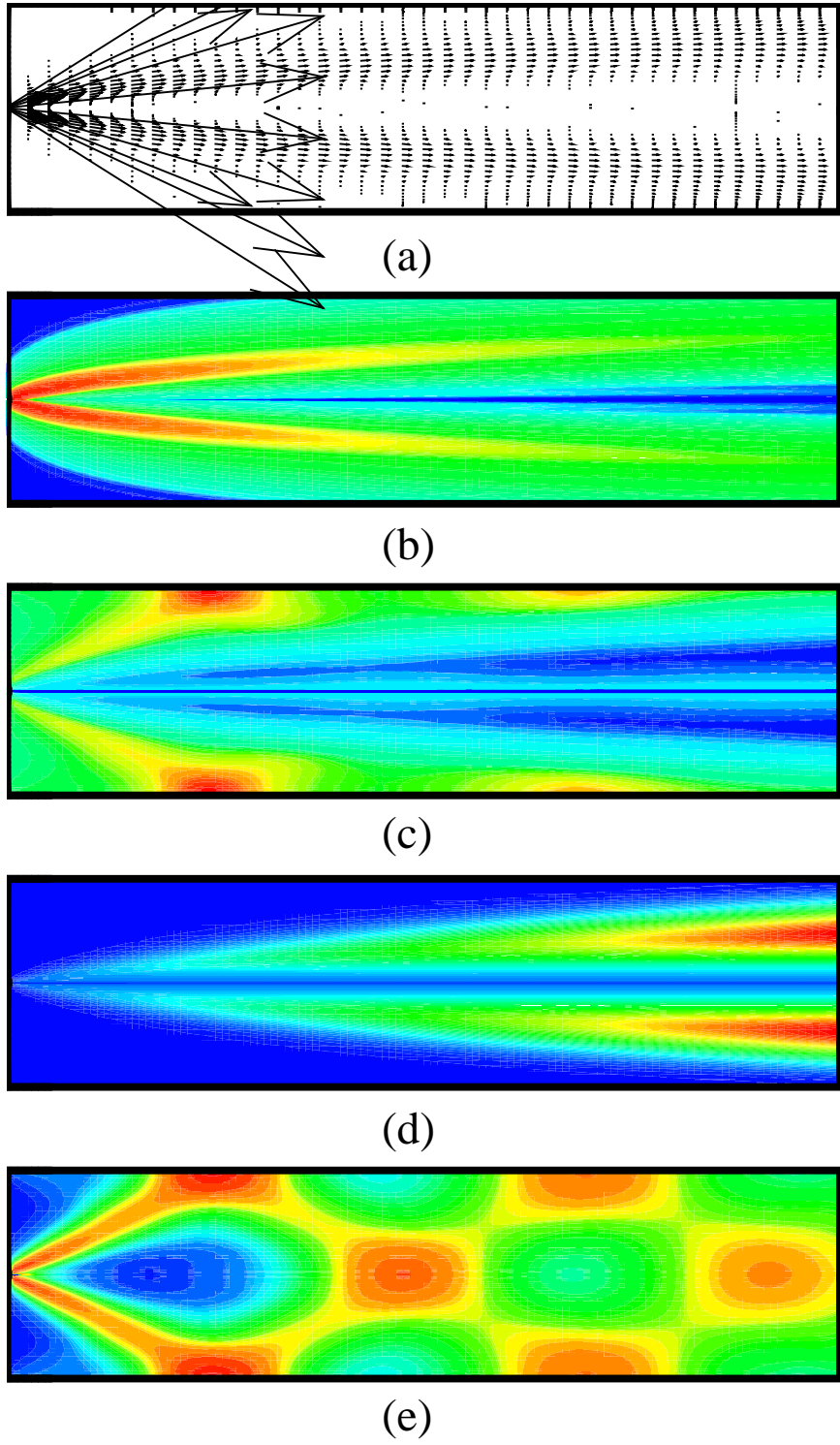


Fig. 10 (a) droplet velocity, (b) droplet volume fraction, (c) gas temperature, (d) mass fraction of water vapor, and (e) pressure distribution over the domain (laminar flow, $M_{in}=2$, $T_{gas,in}=900$ K, $T_{d,in}=300$ K, and $\alpha_d=0.01$).

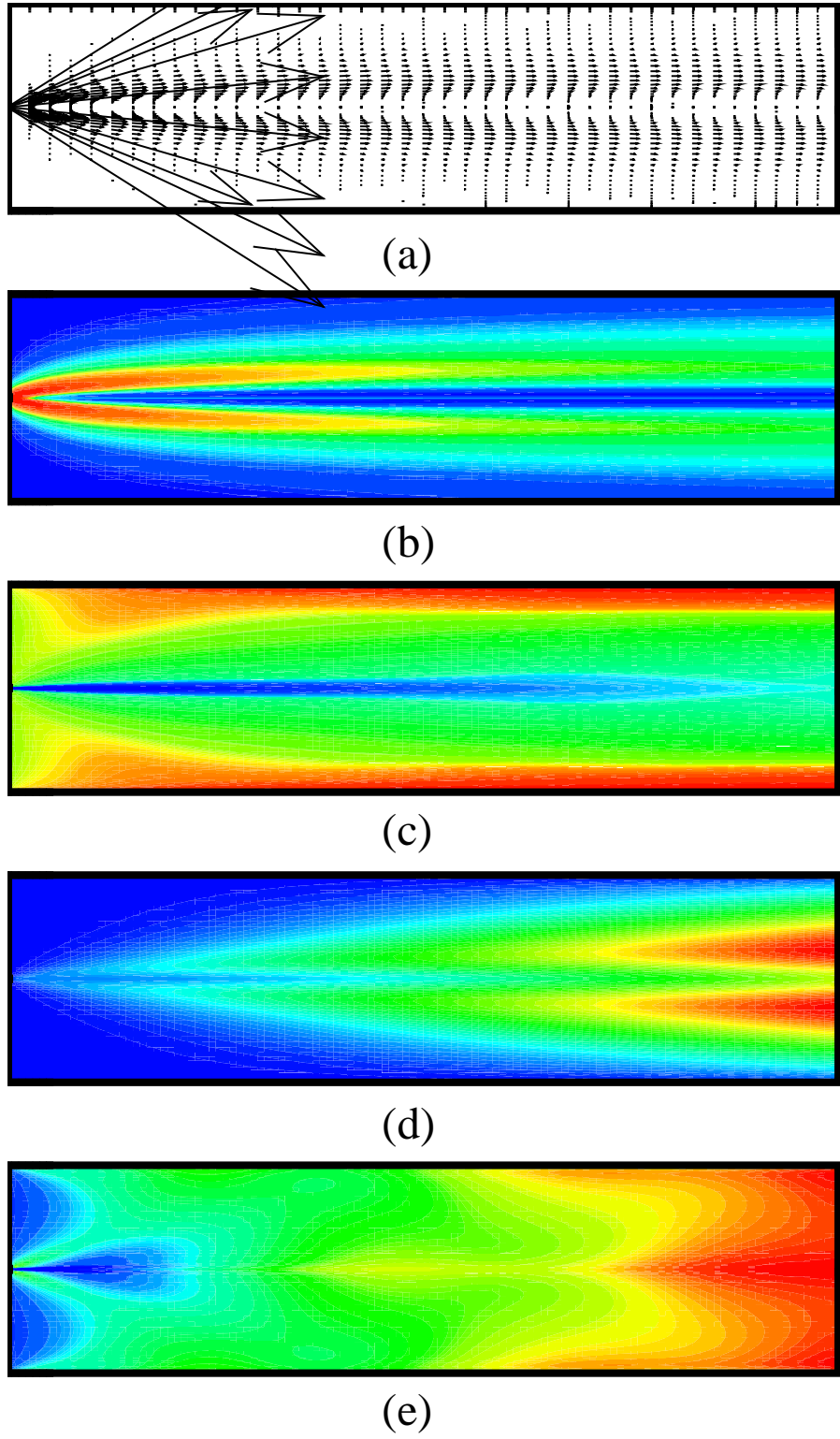


Fig. 11 (a) droplet velocity, (b) droplet volume fraction, (c) gas temperature, (d) mass fraction of water vapor, and (e) pressure distribution over the domain (turbulent flow, k- ϵ model, $M_{in}=2$, $T_{gas,in}=900$ K, $T_{d,in}=300$ K, and $\alpha_d=0.01$).

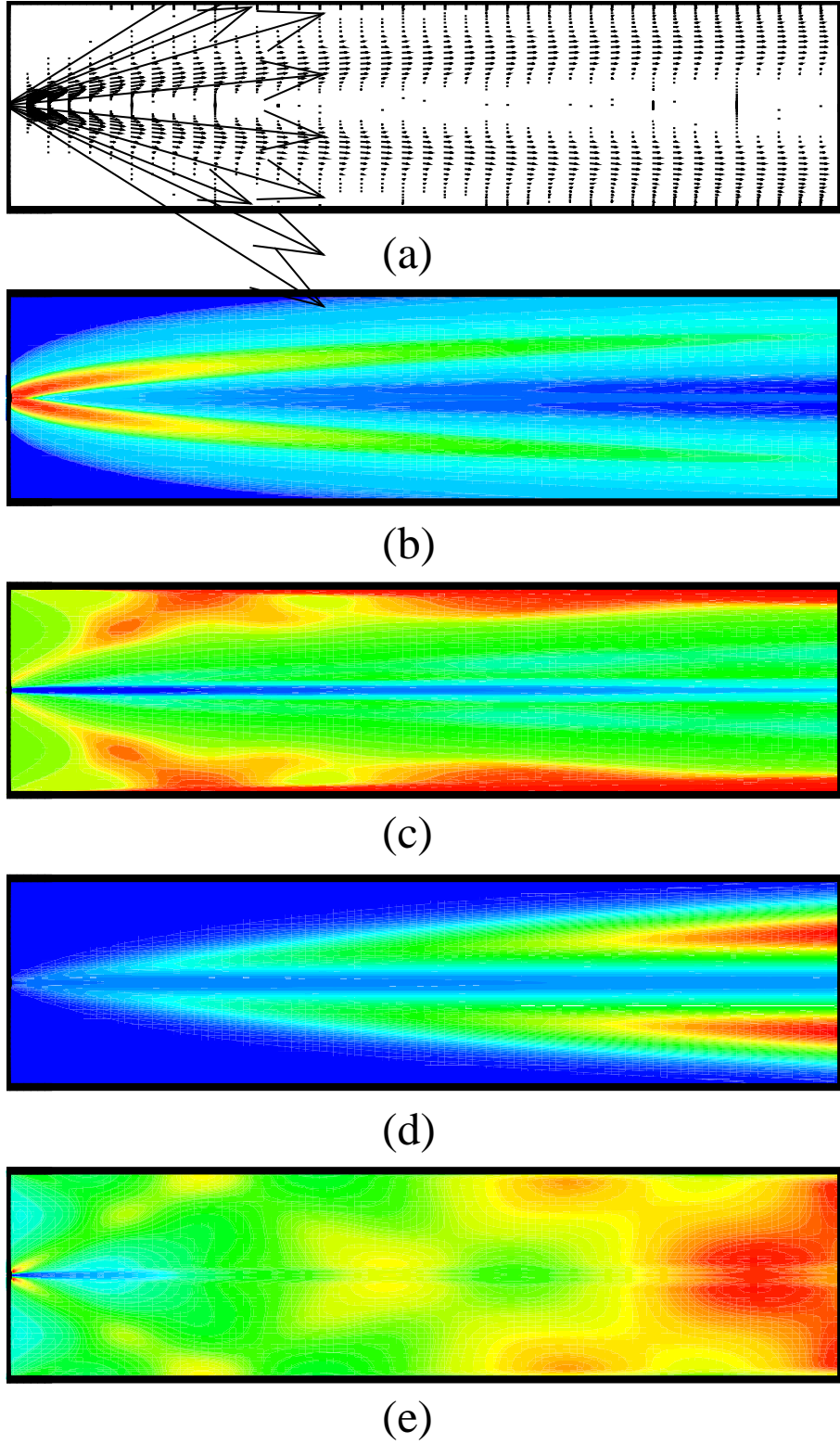


Fig. 12 (a) droplet velocity, (b) droplet volume fraction, (c) gas temperature, (d) mass fraction of water vapor, and (e) pressure distribution over the domain (turbulent flow, $k-\omega$ model, $M_{in}=2$, $T_{gas,in}=900$ K, $T_{d,in}=300$ K, and $\alpha_d=0.01$).

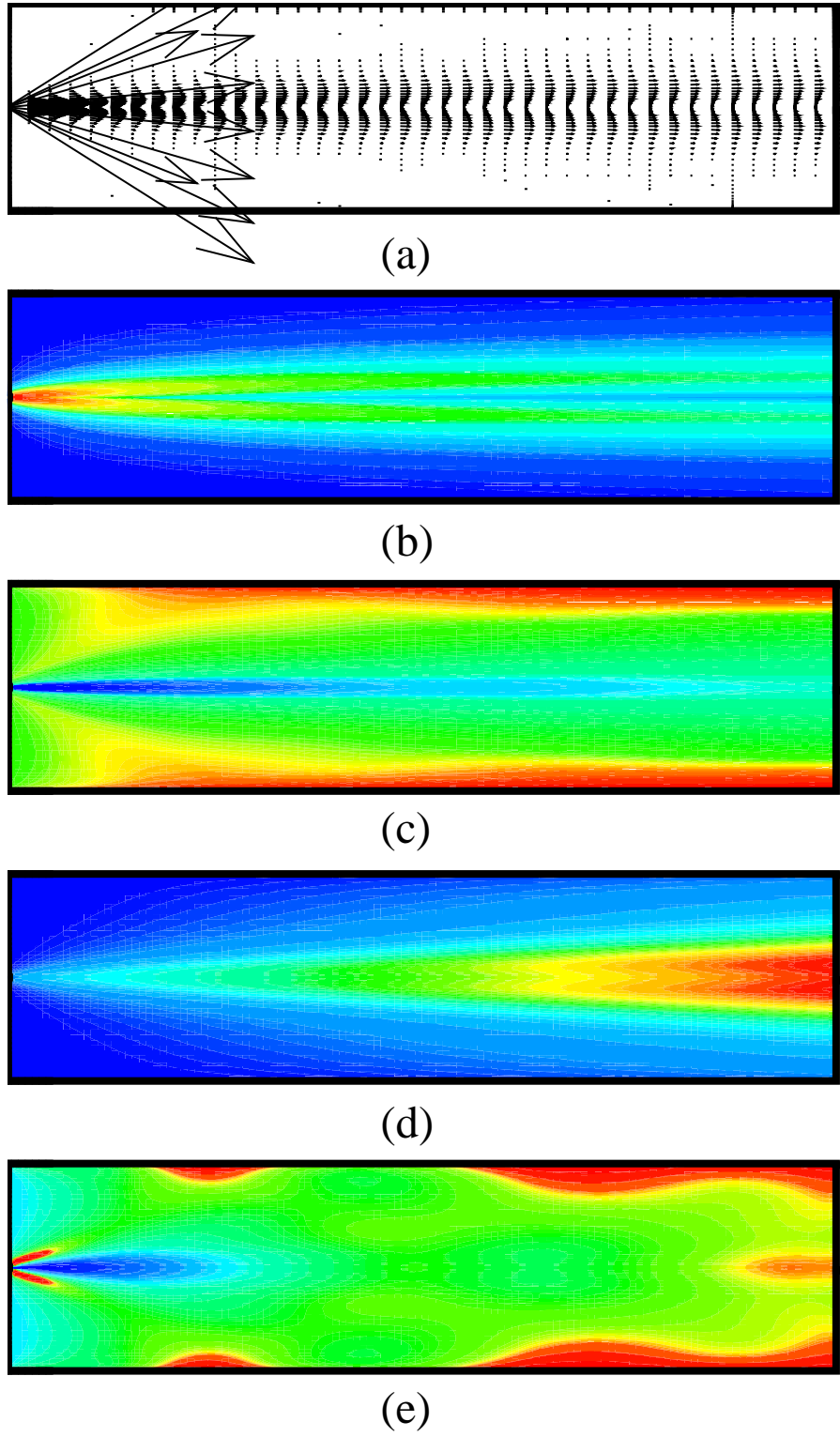


Fig. 13 (a) droplet velocity, (b) droplet volume fraction, (c) gas temperature, (d) mass fraction of water vapor, and (e) pressure distribution over the domain (turbulent flow, SST model, $M_{in}=2$, $T_{gas,in}=900$ K, $T_{d,in}=300$ K, and $\alpha_d=0.01$).

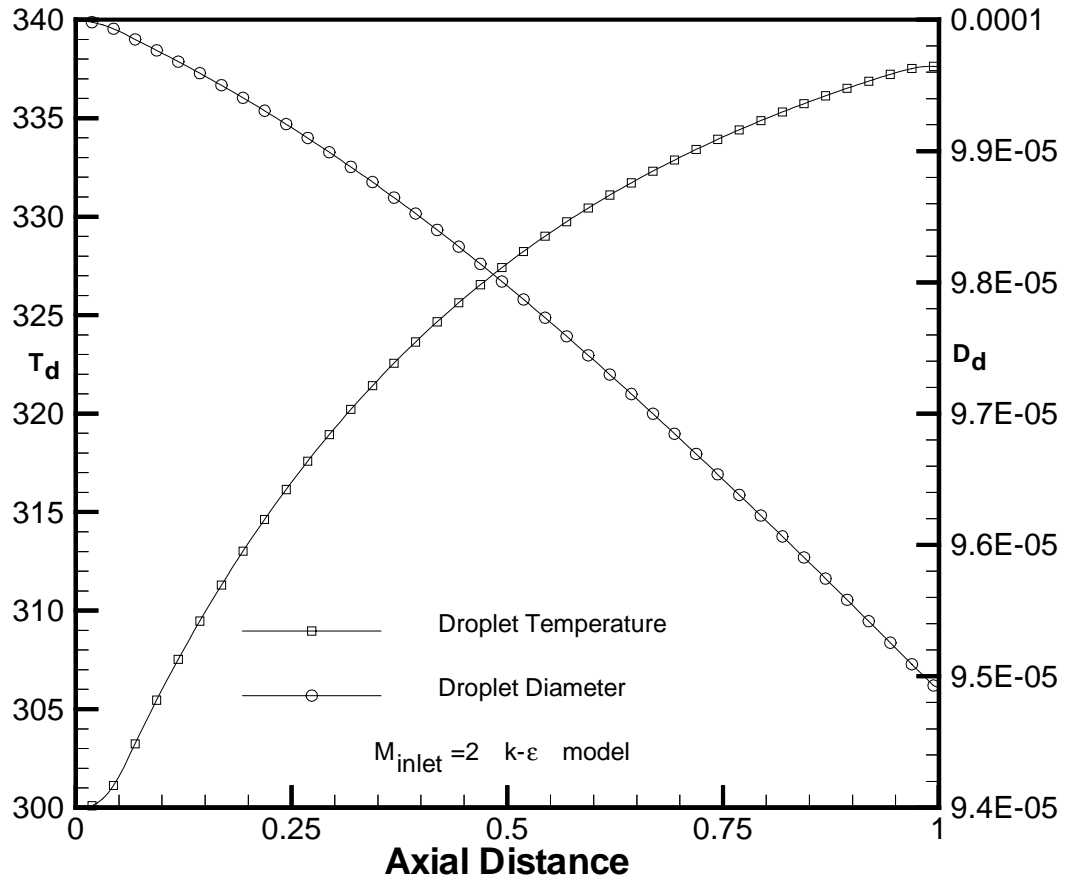


Fig. 14 Variation of droplet temperature and diameter along the center line of the domain (turbulent flow, $k-\epsilon$ model, $M_{in}=2$, $T_{gas,in}=900$ K, $T_{d,in}=300$ K, and $\alpha_d=0.01$).

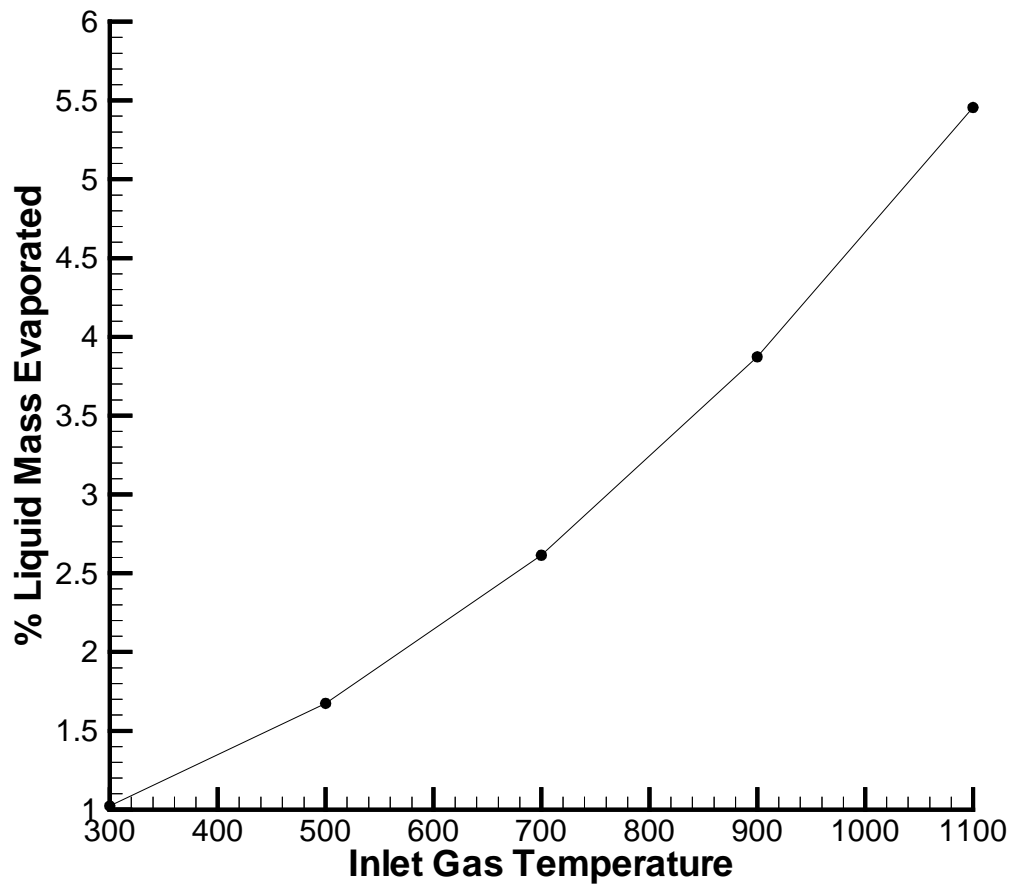


Fig. 15 The percentage, by mass, of the injected liquid droplets that evaporates at different inlet gas temperatures(turbulent flow, SST model, $M_{in}=2$, $T_{d,in}=300$ K, and $\alpha_d=0.01$)..

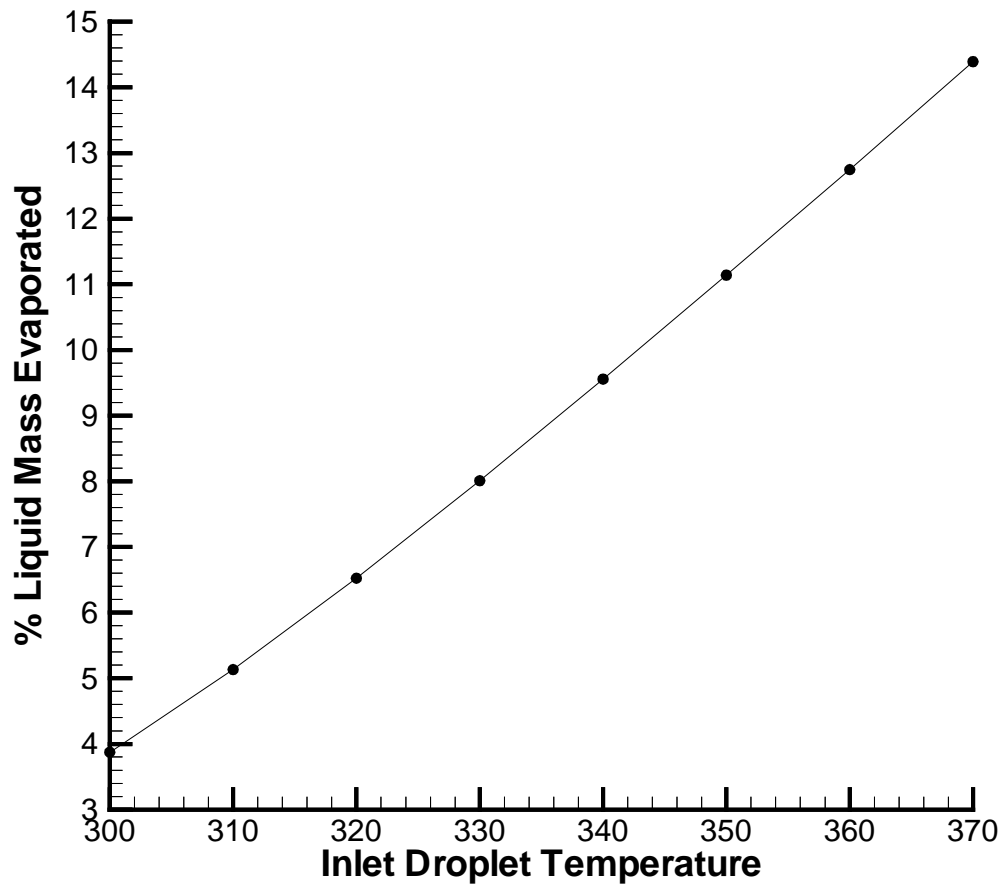


Fig. 16 The percentage, by mass, of the injected liquid droplets that evaporates at different inlet droplet temperature (turbulent flow, SST model, $M_{in}=2$, $T_{gas,in}=900$ K, and $\alpha_d=0.01$)..

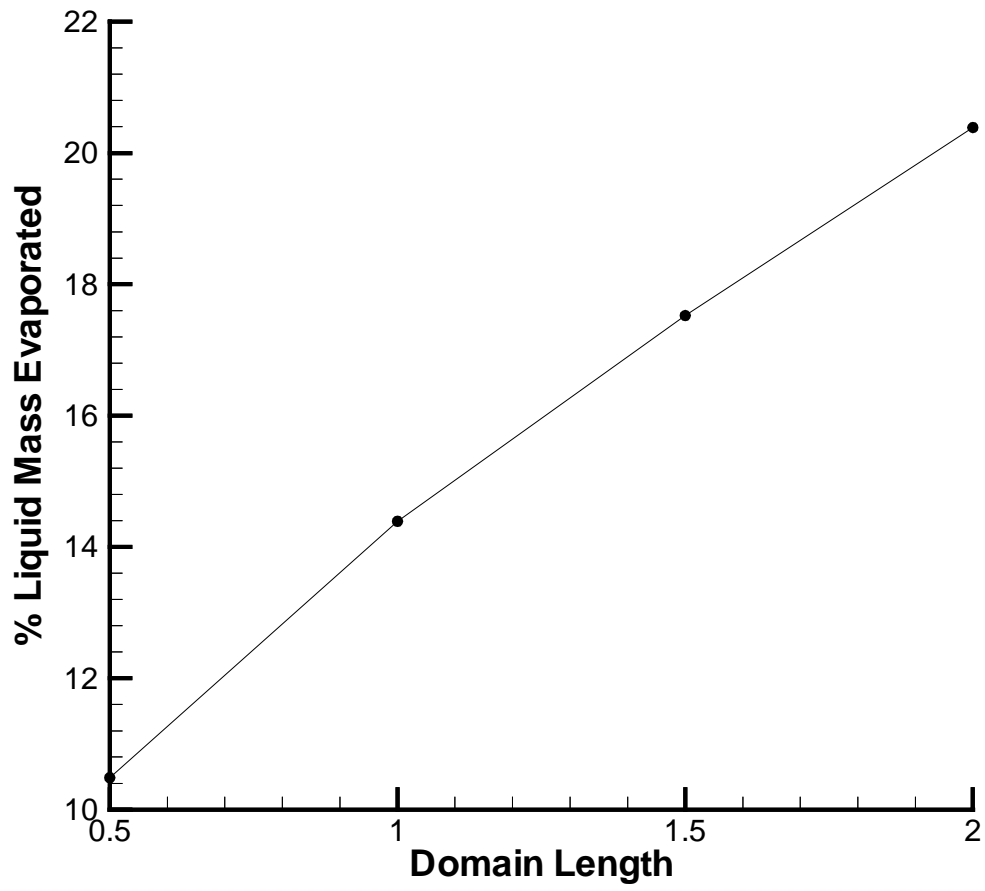
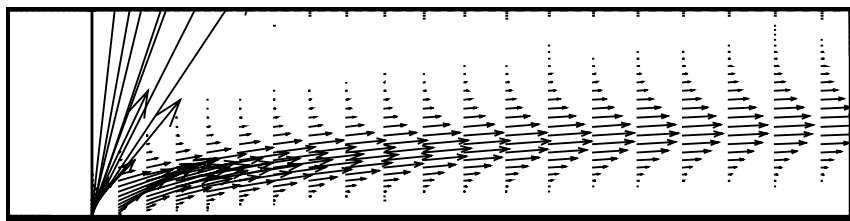
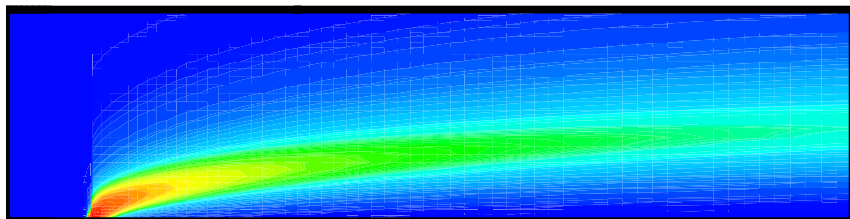


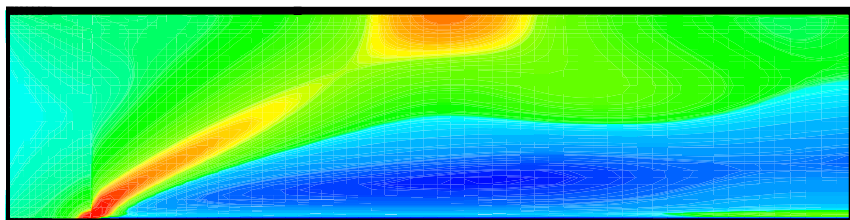
Fig. 17 The percentage, by mass, of the injected liquid droplets that evaporates for different domain length (turbulent flow, k- ϵ model, $M_{in}=2$, $T_{gas,in}=900$ K, $T_{d,in}=370$ K, and $\alpha_d=0.01$).



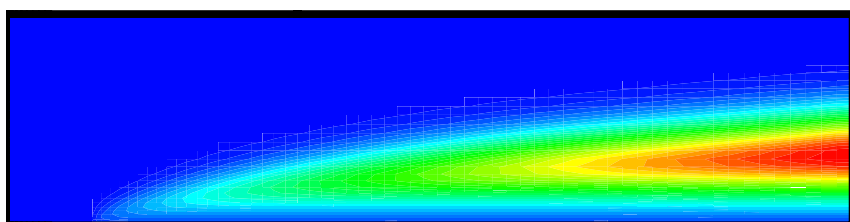
(a)



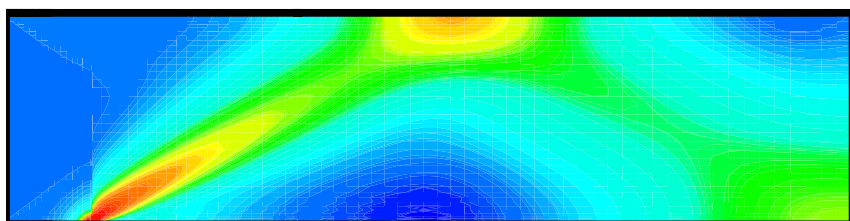
(b)



(c)



(d)



(e)

Fig. 18 (a) droplet velocity, (b) droplet volume fraction, (c) gas temperature, (d) mass fraction of water vapor, and (e) pressure distribution over the domain (laminar $M_{in}=2$, $T_{gas,in}=900$ K, $T_{d,in}=300$ K, and $\alpha_d=0.01$).

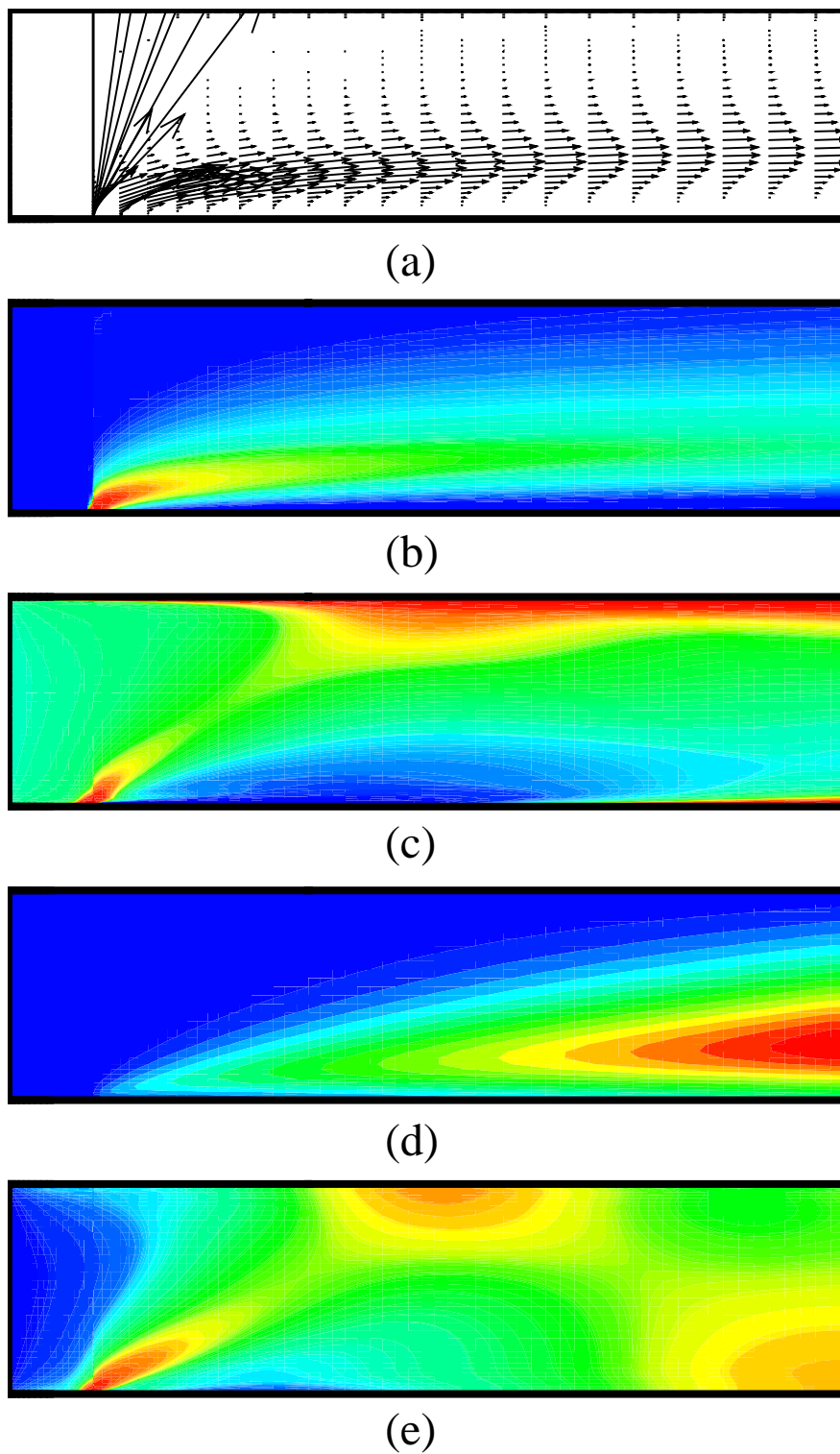


Fig. 19 (a) droplet velocity, (b) droplet volume fraction, (c) gas temperature, (d) mass fraction of water vapor, and (e) pressure distribution over the domain (turbulent flow, k- ϵ model, $M_{in}=2$, $T_{gas,in}=900$ K, $T_{d,in}=300$ K, and $\alpha_d=0.01$).

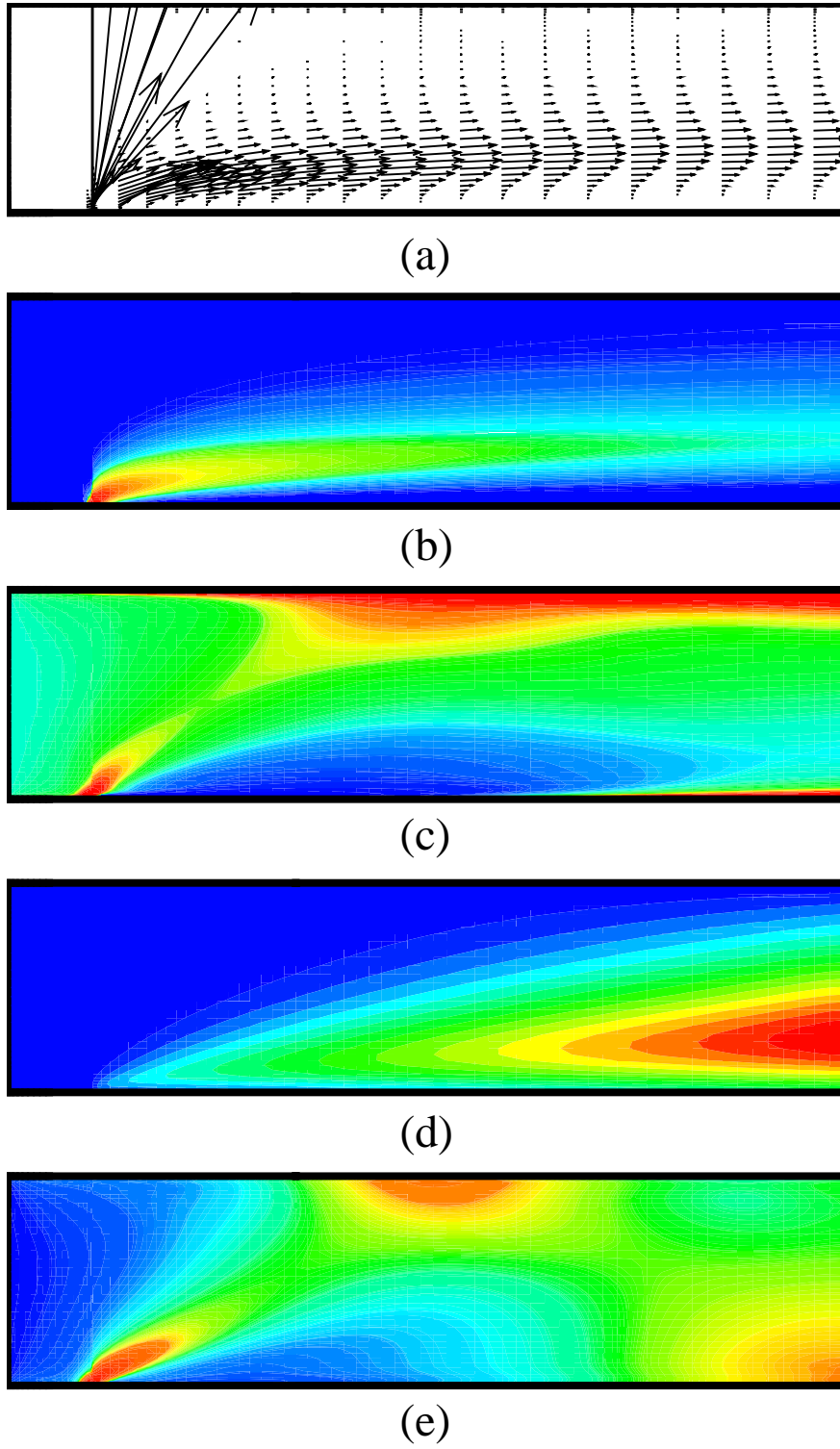


Fig. 20 (a) droplet velocity, (b) droplet volume fraction, (c) gas temperature, (d) mass fraction of water vapor, and (e) pressure distribution over the domain (turbulent flow, $k-\omega$ model, $M_{in}=2$, $T_{gas,in}=900$ K, $T_{d,in}=300$ K, and $\alpha_d=0.01$).

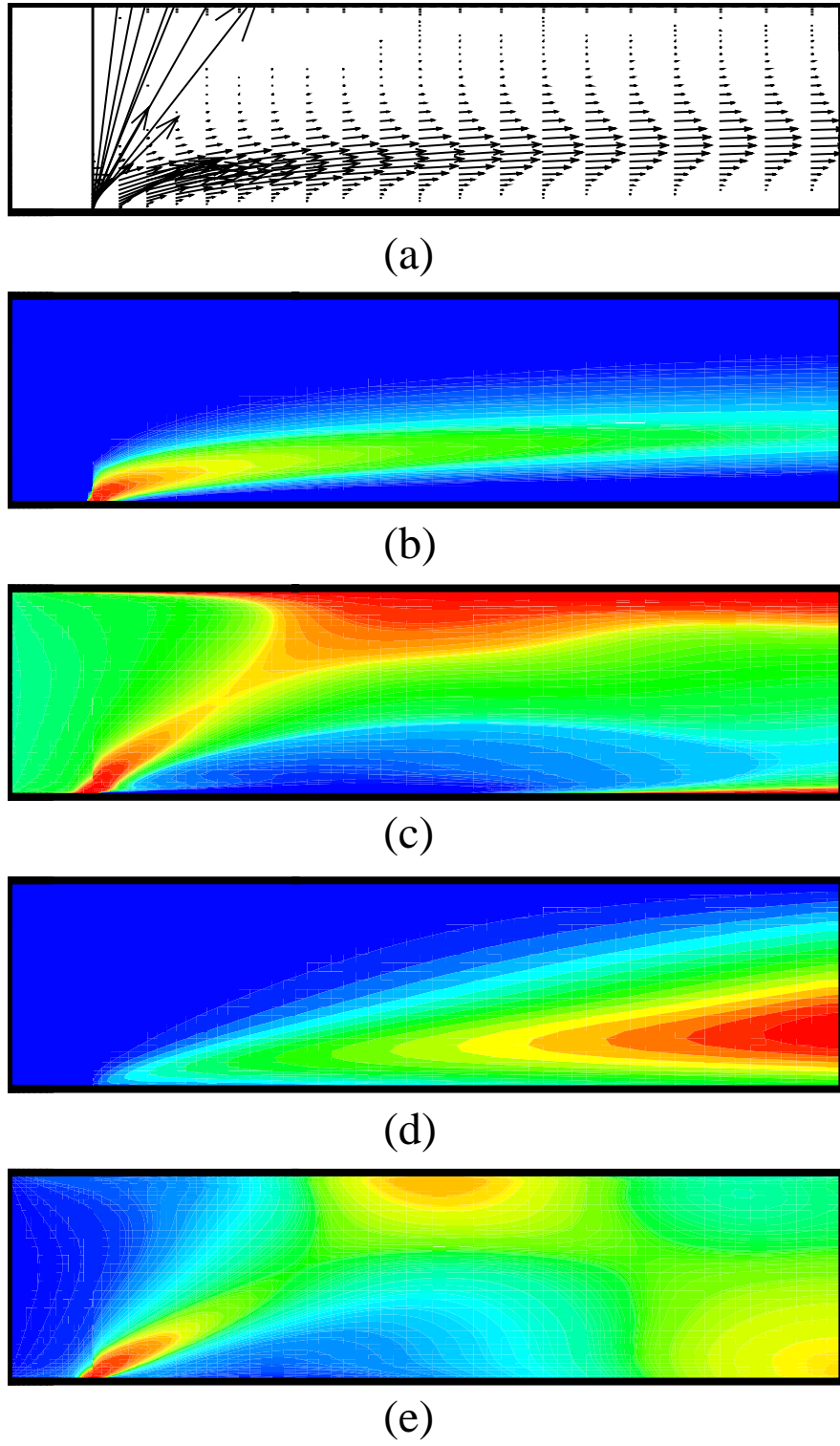


Fig. 21 (a) droplet velocity, (b) droplet volume fraction, (c) gas temperature, (d) mass fraction of water vapor, and (e) pressure distribution over the domain (turbulent flow, SST model, $M_{in}=2$, $T_{gas,in}=900$ K, $T_{d,in}=300$ K, and $\alpha_d=0.01$).

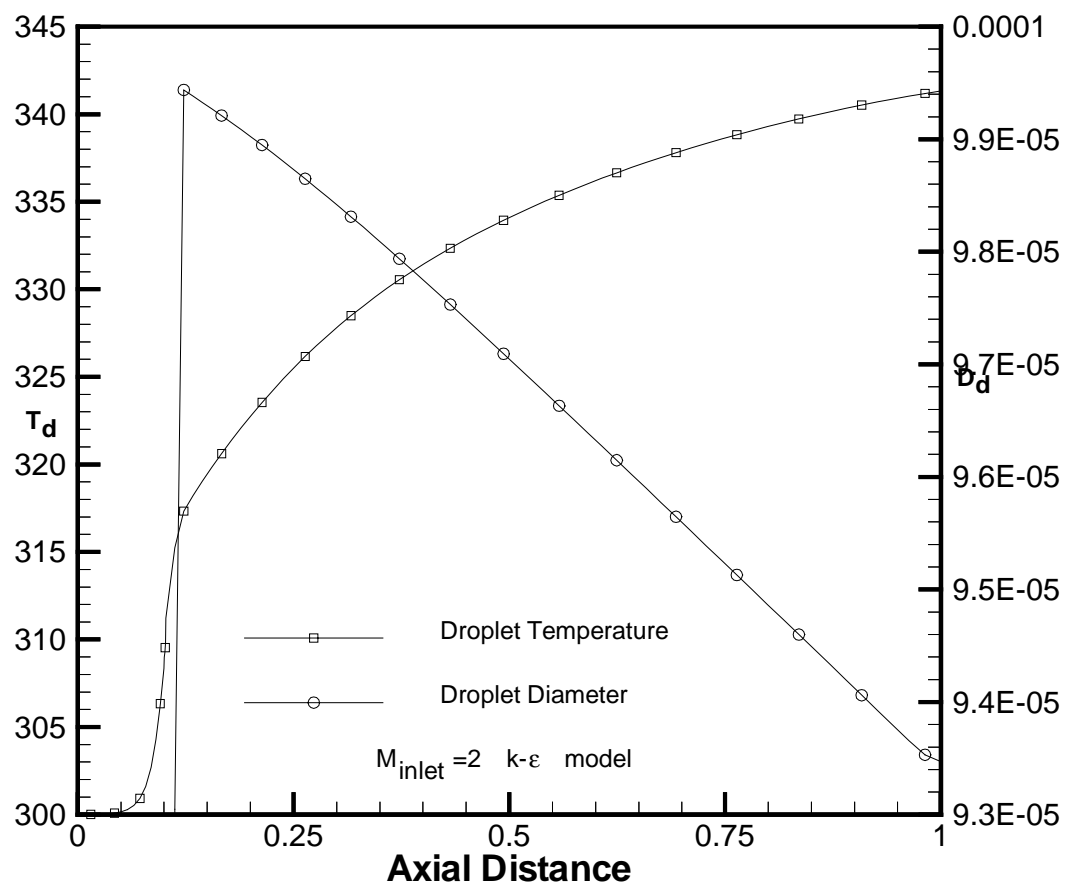


Fig. 22 Variation of droplet temperature and diameter along the center line of the domain (turbulent flow, k- ϵ model, $M_{in}=2$, $T_{gas,in}=900$ K, $T_{d,in}=300$ K, and $\alpha_d=0.01$).

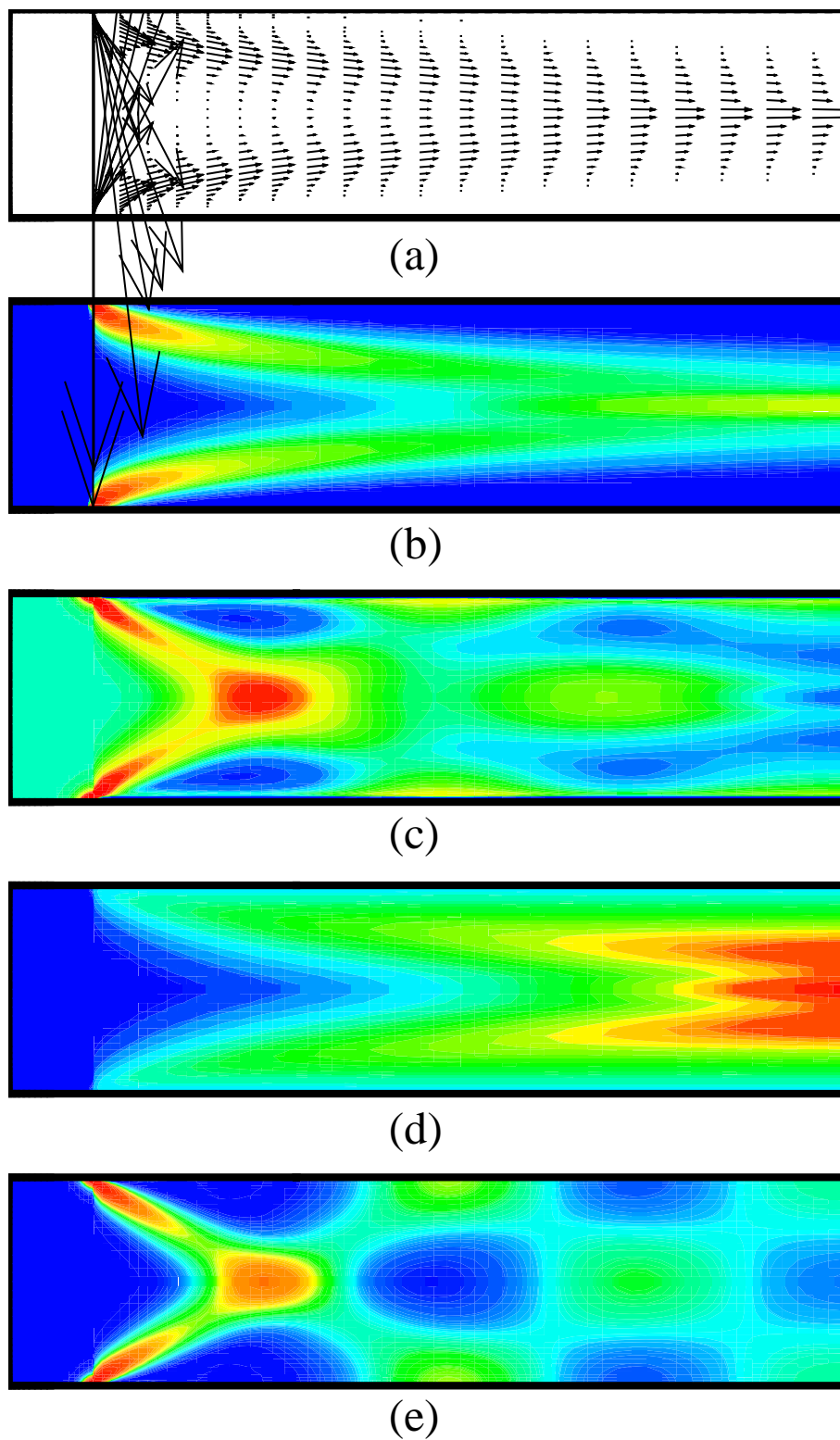


Fig. 23 (a) droplet velocity, (b) droplet volume fraction, (c) gas temperature, (d) mass fraction of water vapor, and (e) pressure distribution over the domain (laminar, $M_{in}=2$, $T_{gas,in}=900$ K, $T_{d,in}=300$ K, and $\alpha_d=0.005$).

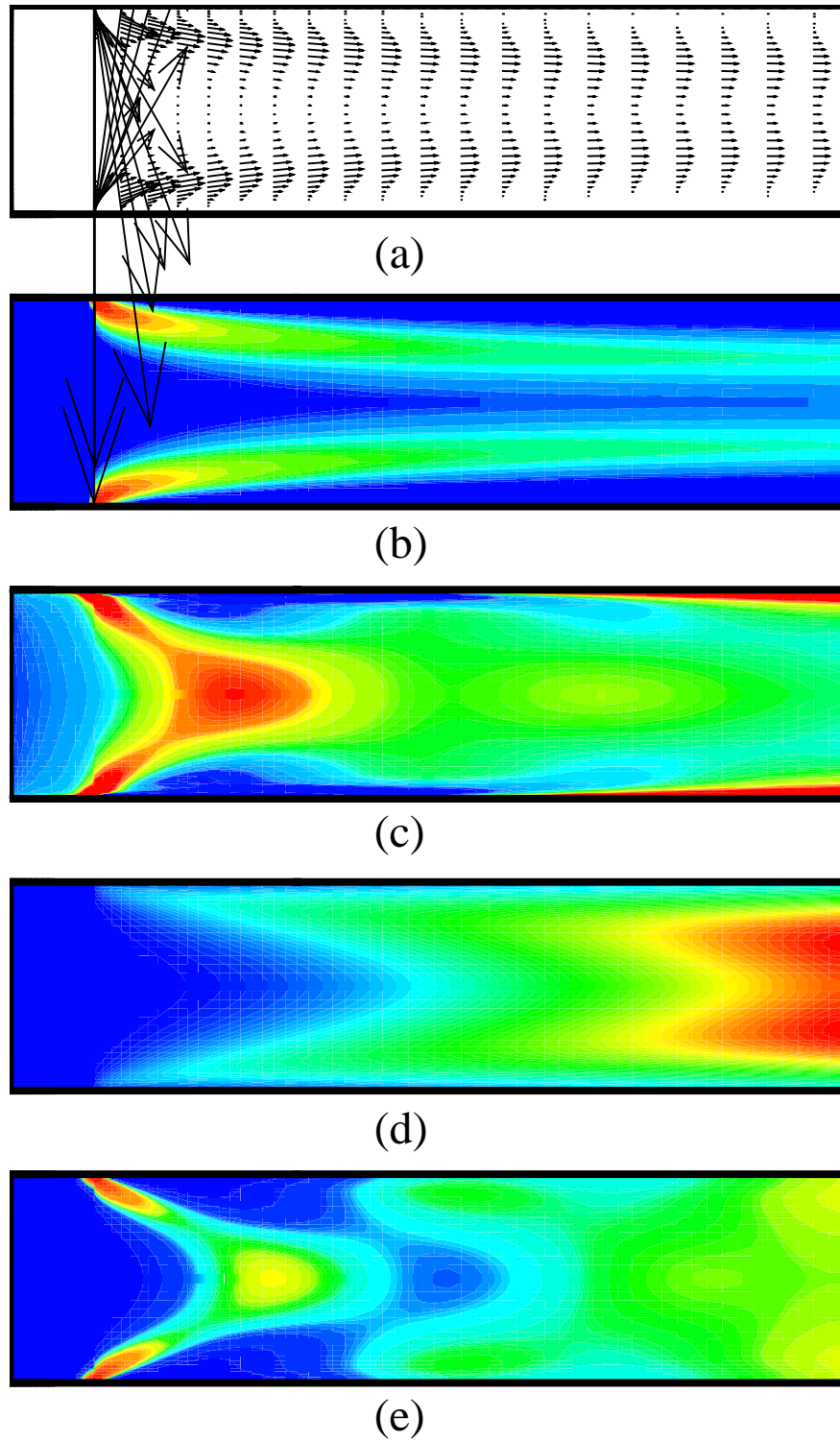


Fig. 24 (a) droplet velocity, (b) droplet volume fraction, (c) gas temperature, (d) mass fraction of water vapor, and (e) pressure distribution over the domain (turbulent flow, $k-\epsilon$ model, $M_{in}=2$, $T_{gas,in}=900$ K, $T_{d,in}=300$ K, and $\alpha_d=0.005$).

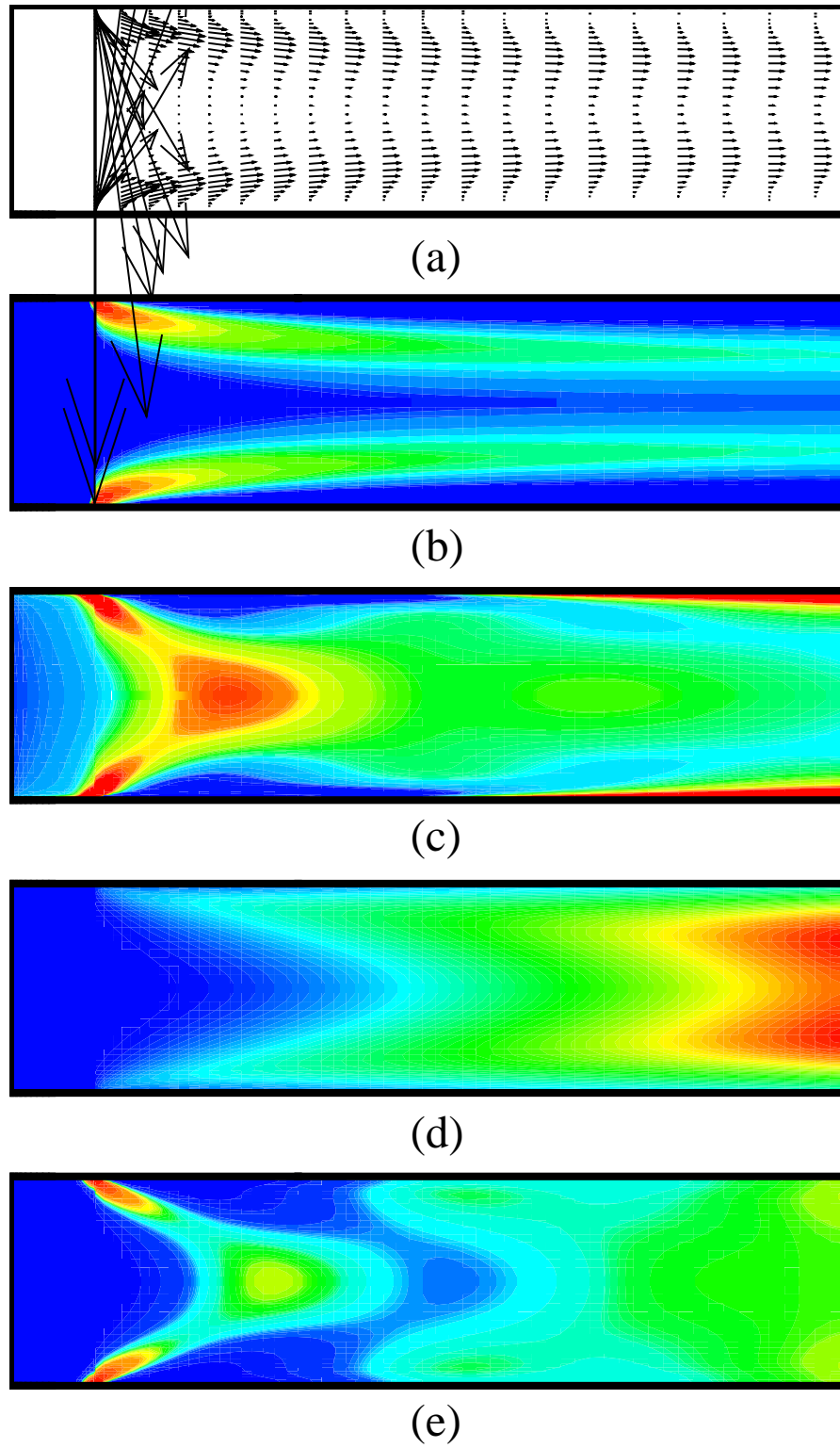


Fig. 25 (a) droplet velocity, (b) droplet volume fraction, (c) gas temperature, (d) mass fraction of water vapor, and (e) pressure distribution over the domain (turbulent flow, $k-\omega$ model, $M_{in}=2$, $T_{gas,in}=900$ K, $T_{d,in}=300$ K, and $\alpha_d=0.005$).

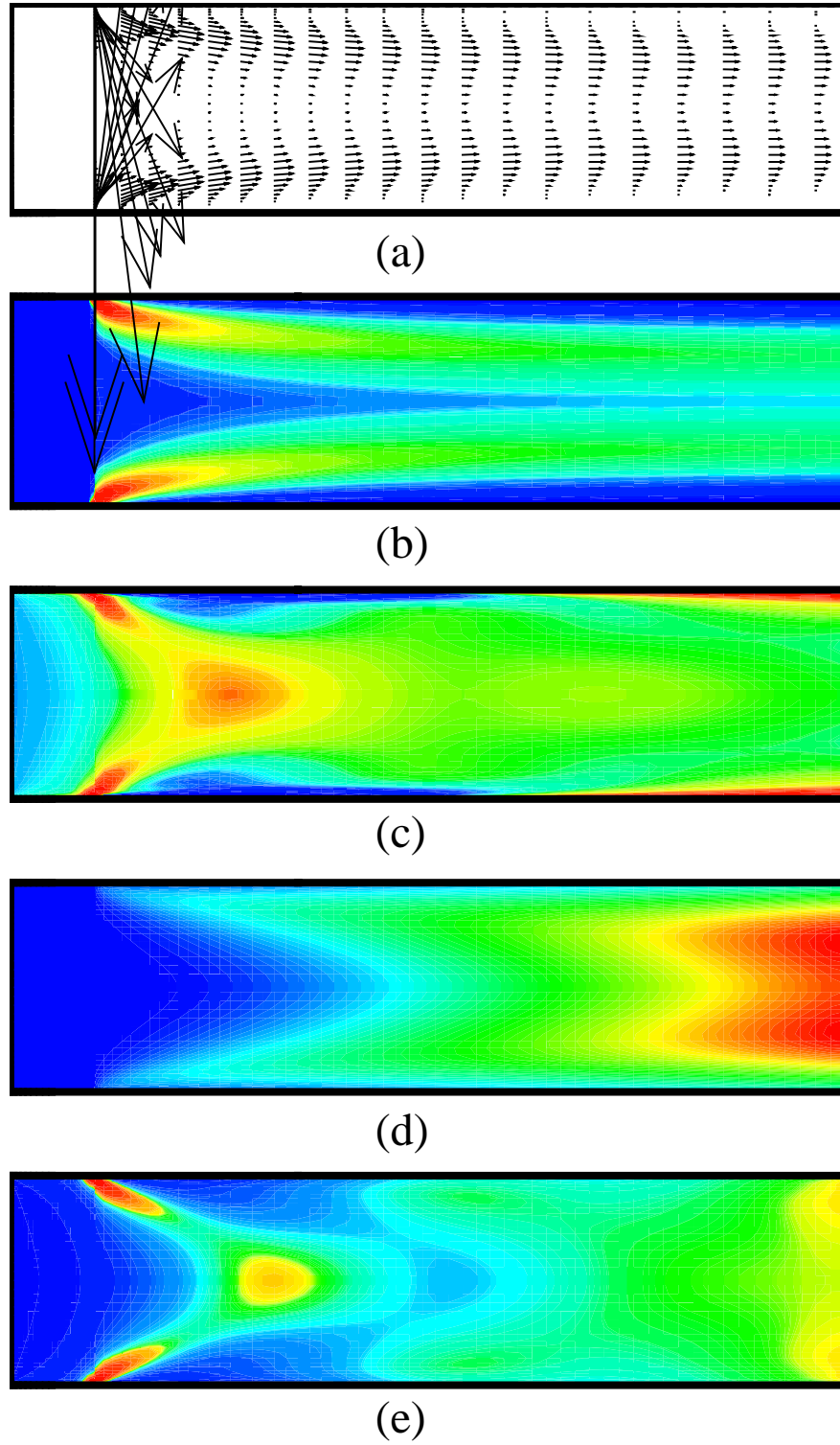


Fig. 26 (a) droplet velocity, (b) droplet volume fraction, (c) gas temperature, (d) mass fraction of water vapor, and (e) pressure distribution over the domain (turbulent flow, SST model, $M_{in}=2$, $T_{gas,in}=900$ K, $T_{d,in}=300$ K, and $\alpha_d=0.005$).

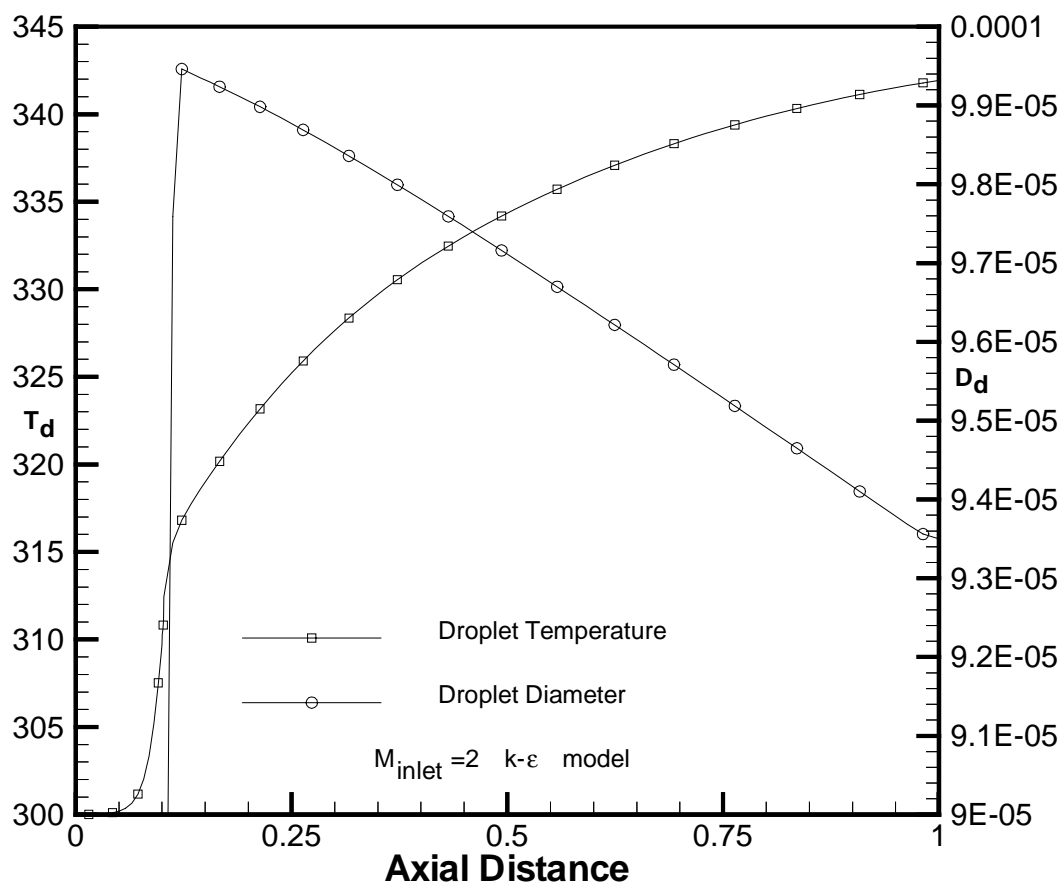


Fig. 27 Variation of droplet temperature and diameter along the center line of the lower half of the domain (turbulent flow, $k-\epsilon$ model, $M_{in}=2$, $T_{gas,in}=900$ K, $T_{d,in}=300$ K, and $\alpha_d=0.005$).